Liquid and Ice Cloud Microphysics in the CSU General Circulation Model. Part III: Sensitivity to Modeling Assumptions

LAURA D. FOWLER AND DAVID A. RANDALL

Department of Atmospheric Science, Colorado State University, Fort Collins, Colorado

(Manuscript received 7 February 1995, in final form 25 August 1995)

ABSTRACT

The inclusion of cloud microphysical processes in general circulation models makes it possible to study the multiple interactions among clouds, the hydrological cycle, and radiation. The gaps between the temporal and spatial scales at which such cloud microphysical processes work and those at which general circulation models presently function force climate modelers to crudely parameterize and simplify the various interactions among the different water species (namely, water vapor, cloud water, cloud ice, rain, and snow) and to use adjustable parameters to which large-scale models can be highly sensitive. Accordingly, the authors have investigated the sensitivity of the climate, simulated with the Colorado State University general circulation model, to various aspects of the parameterization of cloud microphysical processes and its interactions with the cumulus convection and radiative transfer parameterizations.

The results of 120-day sensitivity experiments corresponding to perpetual January conditions have been compared with those of a control simulation in order to 1) determine the importance of advecting cloud water, cloud ice, rain, and snow at the temporal and spatial scale resolutions presently used in the model; 2) study the importance of the formation of extended stratiform anvils at the tops of cumulus towers; 3) analyze the role of mixed-phase clouds in determining the partitioning among cloud water, cloud ice, rain, and snow and, hence, their impacts on the simulated cloud optical properties; 4) evaluate the sensitivity of the atmospheric moisture budget and precipitation rates to a change in the fall velocities of rain and snow; 5) determine the model's sensitivity to the prescribed thresholds of autoconversion of cloud water to rain and cloud ice to snow; and 6) study the impact of the collection of supercooled cloud water by snow, as well as accounting for the cloud optical properties of snow.

Results are presented in terms of 30-day mean differences between the sensitivity experiments and control run. The authors find that three-dimensional advection of the water species has little influence on their geographical distributions and globally averaged amounts. The simulated climate remains unchanged when detrained condensed water at the tops of cumulus towers is used as a source of rain and snow rather than as a source of cloud water and cloud ice. In contrast, instantaneously removing cloud water and cloud ice detrained at the tops of cumulus towers in the form of precipitation yields a strong drying of the atmosphere and a significant reduction in the size of the anvils. Altering the partitioning between cloud ice and supercooled cloud water produces significant changes in the vertical distributions of the cloud optical depth and effective cloud fraction, hence producing significant variations in the top-of-the-atmosphere longwave and shortwave cloud radiative forcings. Increasing the fall speeds of rain and snow leads to a decrease in cloudiness and an increase in stratiform rainfall. Increasing the thresholds for autoconversion of cloud water to rain and cloud ice to snow yields a significant increase in middle- and high-level clouds and a reduction of the cumulus precipitation rate. The collection of supercooled cloud water by snow appeared to be an important microphysical process for mixed-phase clouds. Finally, the optical effects of snow have little impact upon the top-of-the-atmosphere radiation budget.

This study illustrates the need for in-depth analysis of the spatial and temporal scale dependence of the different microphysical parameters of the cloud parameterizations used in general circulation models.

1. Introduction

An increasing number of general circulation models (GCMs) are being endowed with parameterizations of stratiform clouds that include one or more prognostic equations for the mass of cloud water and/or cloud ice. Fowler et al. (1996, hereafter Part I) compiled a list of GCMs that include cloud water and cloud ice parameterizations for stratiform clouds and briefly summarized their parameterized interactions with convection and radiation. The goals of such studies are to improve the parameterizations of cloud microphysical processes in GCMs and to include fundamental couplings between clouds and dynamical processes through three-dimensional advection and diffusion as well as between clouds and the hydrological cycle through precipitation processes. Fowler and Randall (1996, hereafter Part II) described the parameterized interactions between clouds and radiative processes.

Corresponding author address: Dr. Laura D. Fowler, Department of Atmospheric Science, Colorado State University, Fort Collins, CO 80523.

The huge gap between the grid sizes of GCMs and the temporal and spatial scales at which cloud microphysical processes occur forces us to parameterize subgrid-scale cloud microphysical processes (i.e., nucleation, growth of ice crystals and cloud droplets to precipitation particles, collision, and coalescence) using bulk cloud microphysics equations, as first discussed by Kessler (1969). Because bulk cloud microphysics parameterizations have been developed up to now for use in mesoscale models (e.g., Lin et al. 1983; Rutledge and Hobbs 1983, 1984), it is not obvious that they can be readily implemented in large-scale models; at the very least their parameters may have to be adjusted. The autoconversion of cloud water to rain and cloud ice to snow, and its impact on cloudiness and the hydrological cycle, is an example of a scale-dependent parameterization (Fowler and Randall 1994), as discussed later.

The purpose of this paper is to discuss the sensitivity of the climate simulated with the CSU GCM to various assumptions made in the bulk stratiform cloud microphysics parameterization described in Part I and to assumptions relating to the interactions of the parameterized stratiform clouds with the cumulus and radiative transfer parameterizations and with large-scale dynamics. A brief description of the CSU GCM is provided in section 2. In section 3, we discuss the impact of neglecting the advection of cloud water, cloud ice, rain, and snow on the simulated hydrologic cycle and cloudiness. The very important effects of coupling cumulus convection and large-scale condensation through the detrainment of cloud water and cloud ice at the tops of cumulus towers are analyzed in section 4. In section 5, we discuss the contribution of mixed-phase clouds to the atmospheric moisture budget and top-of-the-atmosphere radiation budget. In section 6, we present results of an experiment in which we arbitrarily doubled the fall speeds of rain and snow. In section 7, we analyze the model's sensitivity to the prescribed thresholds for autoconversion of cloud water to rain and cloud ice to snow. Section 8 describes the impact of the collection of supercooled cloud water by snow, as well as the longwave and shortwave radiative effects of snow. Finally, section 9 summarizes our results and suggests possible future improvements to the bulk cloud microphysics parameterization.

2. Design of sensitivity experiments

The CSU GCM has been described in Parts I and II. Briefly, it is a gridpoint model, which in the present study uses a horizontal resolution of 4° latitude by 5° longitude with 17 levels. The vertical discretization is based on a modified σ coordinate in which the planetary boundary layer (PBL) is the bottom layer of the model (Suarez et al. 1983). The cumulus parameterization is a modified version of the Arakawa–Schubert cumulus parameterization (Arakawa and Schubert 1974; Randall and Pan 1993).

TABLE 1. List of experiments. The number associated with each symbol is that used in Fig. 25 to distinguish between the different sensitivity experiments.

Symbol	Experiments
ELQJAN (1)	Control run, similar to that described in Part I and Part II but for perpetual January conditions.
NOADV (2)	No advection of cloud water, cloud ice, rain, or snow.
DETRS (3)	Detrainment at the tops of cumulus towers is used as a source of rain and snow rather than as a source of cloud water and cloud ice.
RAINOUT (4)	Cloud water and cloud ice detrained at the tops of cumulus towers are immediately removed from the atmosphere as stratiform precipitation of rain and snow rather than being used as a source of cloud water and cloud ice.
BERG40 (5)	Cloud water and cloud ice are allowed to coexist in the temperature range $-40°C \leqslant T < 0°C$ instead of $-20°C \leqslant T < 0°C$.
NOBERG (6)	Cloud water and cloud ice are not allowed to coexist. There are no mixed-phase clouds.
FALLRS (7)	The fall speeds of rain and snow are arbitrarily increased by a factor of 2.
QCW0 (8)	The threshold for autoconversion of cloud water to rain is increased from 0.25 to 0.7 g kg^{-1}.
QCI0 (9)	The threshold for autoconversion of cloud ice to snow is increased from 0.01 to 0.03 g kg^{-1}.
PSACW (10)	The collection of supercooled cloud water by snow is neglected.
NORAD (11)	Longwave and shortwave radiative effects of snow are neglected.

As a reminder, the cloud microphysics scheme uses five prognostic equations for the mass of water vapor, cloud water, cloud ice, rain, and snow. Parameterized interactions among the five water species include collection of cloud water (cloud ice) by rain (snow) and explicit time stepping of the precipitation of rain and snow through the atmosphere. Detrainment of cloud water and cloud ice at the tops of cumulus towers serves as a link between cumulus convection and stratiform cloud processes.

The longwave and shortwave radiative transfer parameterizations are described by Harshvardhan et al. (1987, 1989). Cloud optical properties are parameterized as functions of the cloud water, cloud ice, and snow paths, while the optical effects of rain are neglected. As explained in Part II, the CSU GCM does not include fractional cloudiness at this time, except for PBL clouds. The amount of free-tropospheric clouds is set equal to 1, if the total amount of condensate exceeds 10^{-5} kg kg^{-1}, and equal to 0, otherwise. For simplicity, we will use the term *cloud fraction* to describe the fraction of clouds in the PBL and the frequency of occurrence of clouds in the free troposphere.

TABLE 2. Globally averaged values of hydrologic quantities and rates as simulated in the runs listed in Table 1.

Hydrologic cycle quantities and rates	ELQJAN	NOADV	DETRS	RAINOUT	FALLRS	BERG40	NOBERG	QCW0	QCI0	PSACW	NORAD
Water vapor (kg m^{-2})	23.31	22.65	22.39	20.07	22.79	23.70	23.21	23.43	24.70	23.43	23.23
Cloud water (kg m^{-2})	0.044	0.044	0.042	0.044	0.049	0.050	0.041	0.075	0.047	0.097	0.045
Cloud ice (kg m^{-2})	0.019	0.018	0.014	0.011	0.019	0.018	0.021	0.019	0.031	0.021	0.019
Rain (kg m^{-2})	0.016	0.015	0.015	0.012	0.009	0.017	0.016	0.017	0.018	0.017	0.016
Snow (kg m^{-2})	0.135	0.121	0.146	0.086	0.065	0.144	0.134	0.141	0.126	0.144	0.137
Cumulus precipitation (mm day^{-1})	1.72	1.76	1.90	1.84	1.62	1.61	1.74	1.69	1.44	1.67	1.69
Large-scale precipitation of rain (mm day^{-1})	1.34	1.36	1.28	1.29	1.45	1.35	1.34	1.38	1.40	1.35	1.36
Large-scale precipitation of snow (mm day^{-1})	0.62	0.64	0.65	1.03	0.65	0.61	0.64	0.64	0.56	0.62	0.65
Total large-scale precipitation (mm day^{-1})	1.96	2.00	1.93	2.32	2.10	1.96	1.98	2.02	1.96	1.97	2.01
Total precipitation (mm day^{-1})	3.68	3.76	3.83	4.16	3.72	3.57	3.72	3.71	3.40	3.63	3.70

All simulations described in this paper were run for perpetual January conditions corresponding to 15 January of the annual cycle simulation described in Parts I and II and are 120 days long. The results presented here correspond to averages over the last 30 days of each simulation. While formal statistical tests were not performed, the differences described in this paper were large compared to the temporal and spatial variations evident in the simulations. Time series of several variables, such as cloud water and cloud ice, did not reveal any systematic drift in the climate experiments. Also, difference plots of variables averaged between days 61 and 90 and days 91 and 120 did not exhibit major biases that would alter the validity of our results.

The climate simulation hereafter referred to as ELQJAN uses the same version of the model as EAULIQ in Parts I and II and will serve as the reference or "control" simulation. The January climates obtained with EAULIQ and ELQJAN are very similar, although EAULIQ is an annual cycle simulation, and ELQJAN uses fixed top-of-the-atmosphere insolation and surface boundary conditions. ELQJAN produces a partitioning between water vapor, cloud water, cloud ice, rain, and snow that is very similar to that obtained with EAULIQ and, in particular, gives comparable geographical distributions of the planetary radiation budget and cloudiness. Therefore, we refer the reader to Parts I and II for a description of the simulated January climate.

TABLE 3. Globally averaged values of planetary radiation budget quantities as simulated in the runs listed in Table 1.

Radiation budget quantities	ELQJAN	NOADV	DETRS	RAINOUT	FALLRS	BERG40	NOBERG	QCW0	QCI0	PSACW	NORAD
Outgoing infrared radiation (W m^{-2})	226.98	231.01	233.63	249.42	229.67	220.88	229.17	226.37	213.30	222.09	229.30
Planetary albedo (%)	33.56	32.78	31.81	29.87	33.34	34.86	32.63	35.00	36.20	38.08	32.61
Absorbed shortwave radiation (W m^{-2})	234.36	237.12	240.53	247.39	235.14	229.79	237.74	229.41	224.94	218.41	237.69
Clear-sky outgoing infrared radiation (W m^{-2})	260.87	262.12	261.66	267.29	261.74	261.15	261.04	260.75	261.18	260.74	261.02
Clear-sky absorbed shortwave radiation (W m^{-2})	299.88	299.61	299.27	299.13	299.31	299.49	299.24	299.39	299.52	299.97	299.38
Longwave cloud radiative forcing (W m^{-2})	33.89	31.11	28.03	17.87	32.07	40.27	31.87	34.38	47.88	38.65	31.72
Shortwave cloud radiative forcing (W m^{-2})	−65.52	−62.49	−58.73	−51.74	−64.17	−69.71	−61.60	−69.98	−74.58	−81.56	−61.69
Net cloud radiative forcing (W m^{-2})	−31.63	−31.38	−30.70	−33.87	−32.10	−29.44	−29.73	−35.60	−26.70	−42.91	−29.97
Atmospheric radiative cooling (W m^{-2})	113.38	115.29	117.85	129.79	114.66	110.09	113.09	113.50	104.43	112.26	114.03

TABLE 4. Globally averaged total, high-, middle,- and low-level cloud amounts as simulated in the runs listed in Table 1.

Cloud amount (%)	ELQJAN	NOADV	DETRS	RAINOUT	FALLRS	BERG40	NOBERG	QCW0	QCI0	PSACW	NORAD
Total cloud amount	70.98	64.39	69.98	50.97	66.11	72.33	70.37	71.92	78.60	73.60	66.21
Total effective cloud amount	44.05	40.72	40.68	35.20	41.90	48.26	41.84	45.62	54.38	50.08	41.35
High-level cloud amount	52.98	44.52	52.23	25.57	46.87	54.94	52.61	53.15	66.01	53.78	48.03
Middle-level cloud amount	30.06	25.51	30.98	22.38	25.19	30.96	29.57	31.29	30.28	33.19	15.69
Low-level cloud amount	33.03	31.09	32.74	32.75	31.34	32.51	33.45	34.56	32.85	35.60	28.30

In the following sections, the water vapor, cloud water, cloud ice, rain, and snow mixing ratios will be referred to as WV, CW, CI, RW, and RI, respectively. We will use C, C_{ef}, and τ to denote the simulated cloud fraction, the effective cloud fraction, and the cloud optical depth, respectively. The effective cloud fraction is defined as the cloud fraction times the cloud infrared emissivity. Because the infrared emissivity of clouds has a value between 0 and 1, so does C_{ef}, although the cloud amount in the free troposphere can only be 0 or 1. The outgoing longwave radiation and planetary albedo will be referred to as OLR and α. LWCRF and SWCRF will be used as acronyms for the top-of-the-atmosphere longwave and shortwave cloud radiative forcings, respectively.

Table 1 gives a list of the various sensitivity experiments that we have conducted. Tables 2–4 summarize the globally averaged values of the atmospheric moisture budget, planetary radiation budget, and cloud amounts obtained in the various simulations listed in Table 1.

3. Advection of condensed water

In the NOADV simulation, we neglect the horizontal and vertical advection of cloud water, cloud ice, rain,

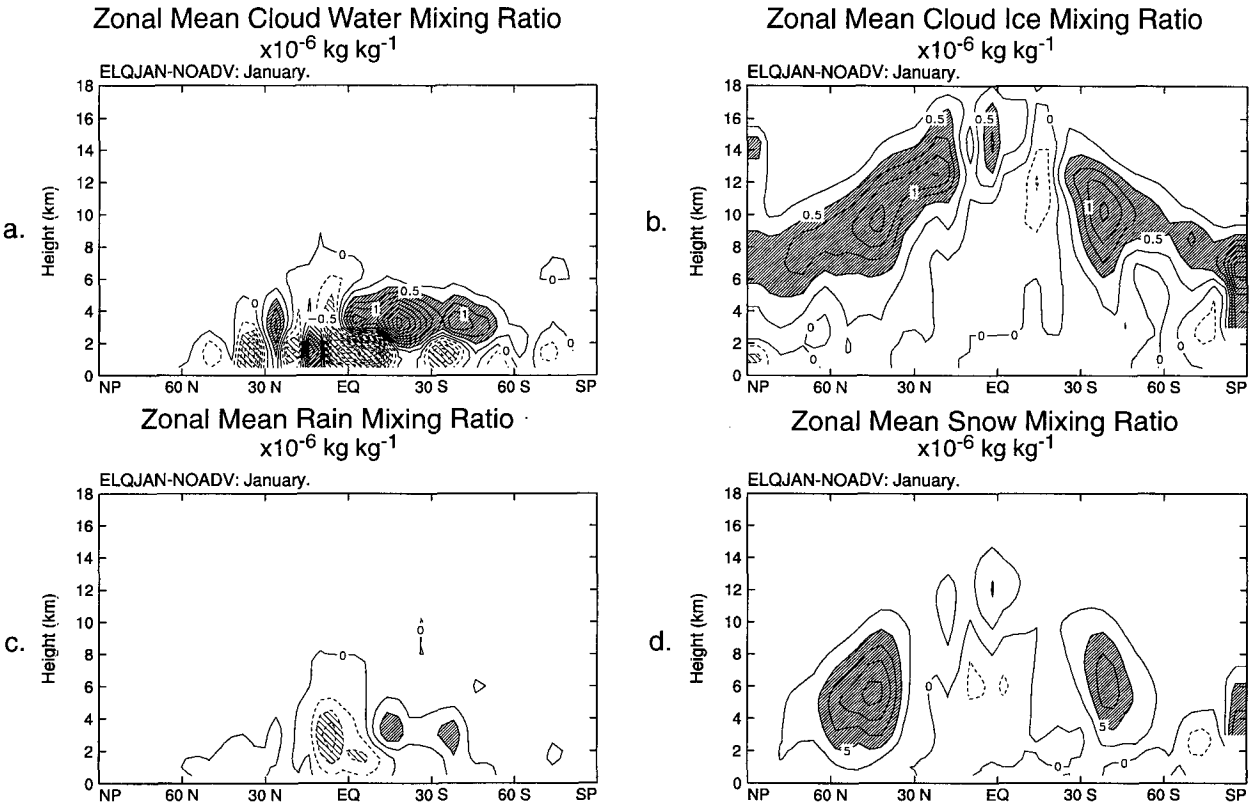

FIG. 1. Latitude–height cross sections of the zonally averaged differences in (a) the cloud water, (b) cloud ice, (c) rain, and (d) snow mixing ratios between ELQJAN and NOADV. In (a), (b), and (c) contour intervals are every 0.25×10^{-6} kg kg^{-1}. Light shading corresponds to values less than -0.5×10^{-6} kg kg^{-1}, and heavy shading corresponds to values greater than 0.5×10^{-6} kg kg^{-1}. In (d) contour intervals are every 2.5×10^{-6} kg kg^{-1}. Heavy shading corresponds to values greater than 5×10^{-6} kg kg^{-1}.

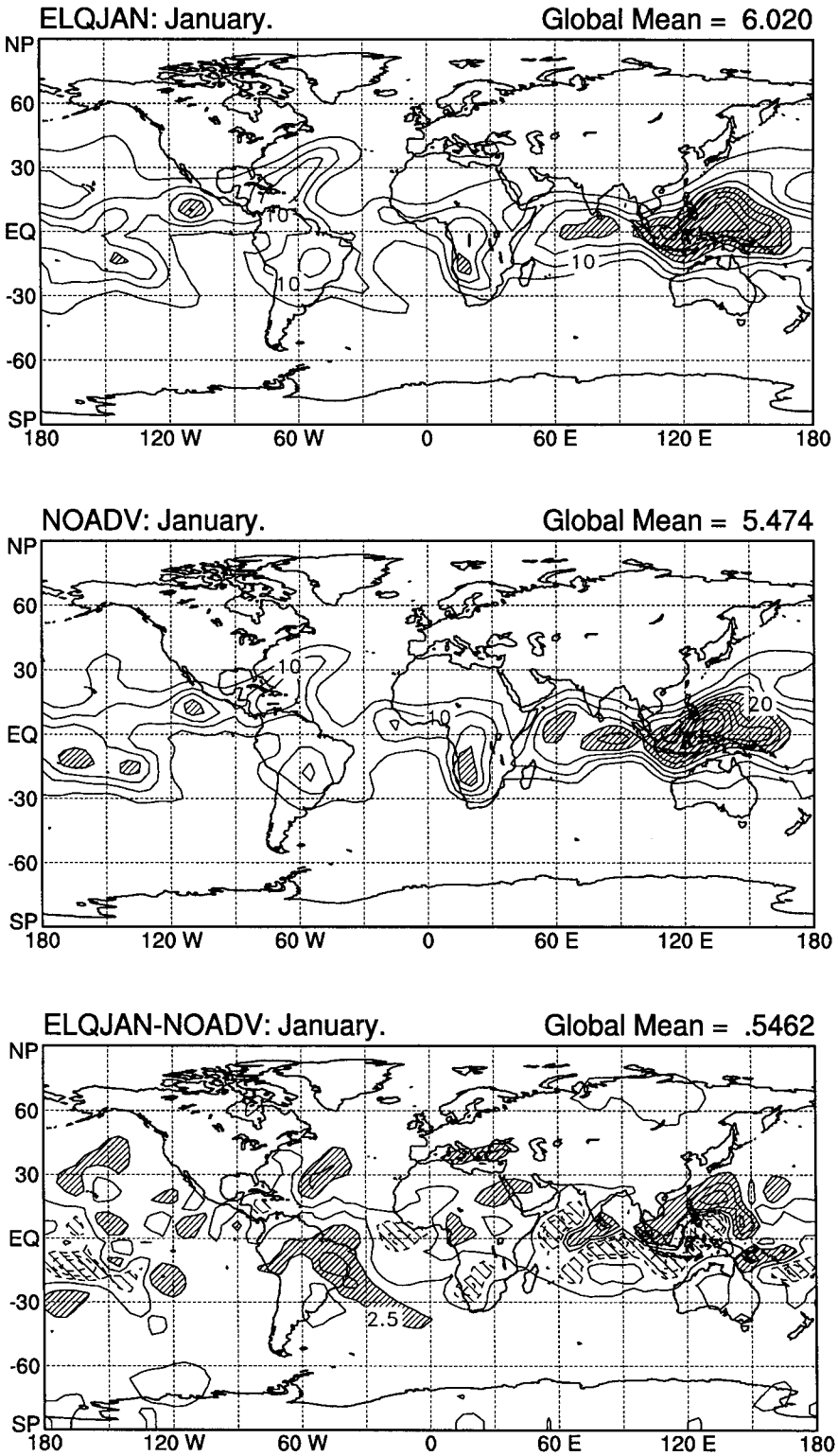

FIG. 2. Global maps of the cloud ice mixing ratio at 200 mb simulated by (a) ELQJAN, (b) NOADV, and (c) its difference ELQJAN minus NOADV. In (a) and (b) contour intervals are every 5×10^{-6} kg kg^{-1}. Heavy shading corresponds to values greater than 20×10^{-6} kg kg^{-1}. In (c) contour intervals are every 2.5×10^{-6} kg kg^{-1}. Light shading corresponds to values less than -2.5×10^{-6} kg kg^{-1}, and heavy shading corresponds to values greater than 2.5×10^{-6} kg kg^{-1}.

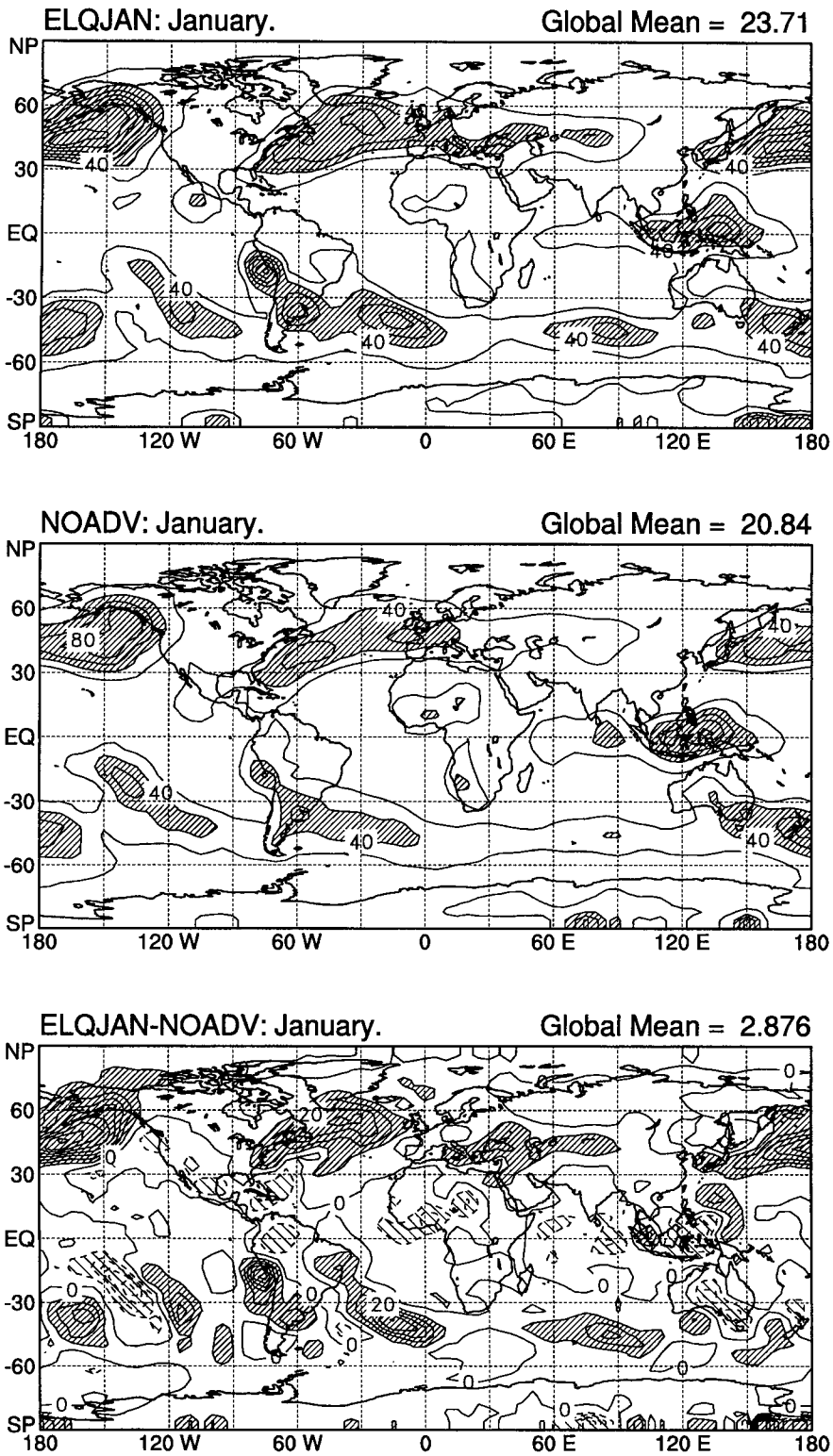

FIG. 3. Global maps of the snow mixing ratio at 500 mb simulated by (a) ELQJAN, (b) NOADV, and (c) its difference ELQJAN minus NOADV. In (a) and (b) contour intervals are every 20×10^{-6} kg kg^{-1}. Heavy shading corresponds to values greater than 40×10^{-6} kg kg^{-1}. In (c) contour intervals are every 10×10^{-6} kg kg^{-1}. Light shading corresponds to values less than -10×10^{-6} kg kg^{-1}, and heavy shading corresponds to values greater than 10×10^{-6} kg kg^{-1}.

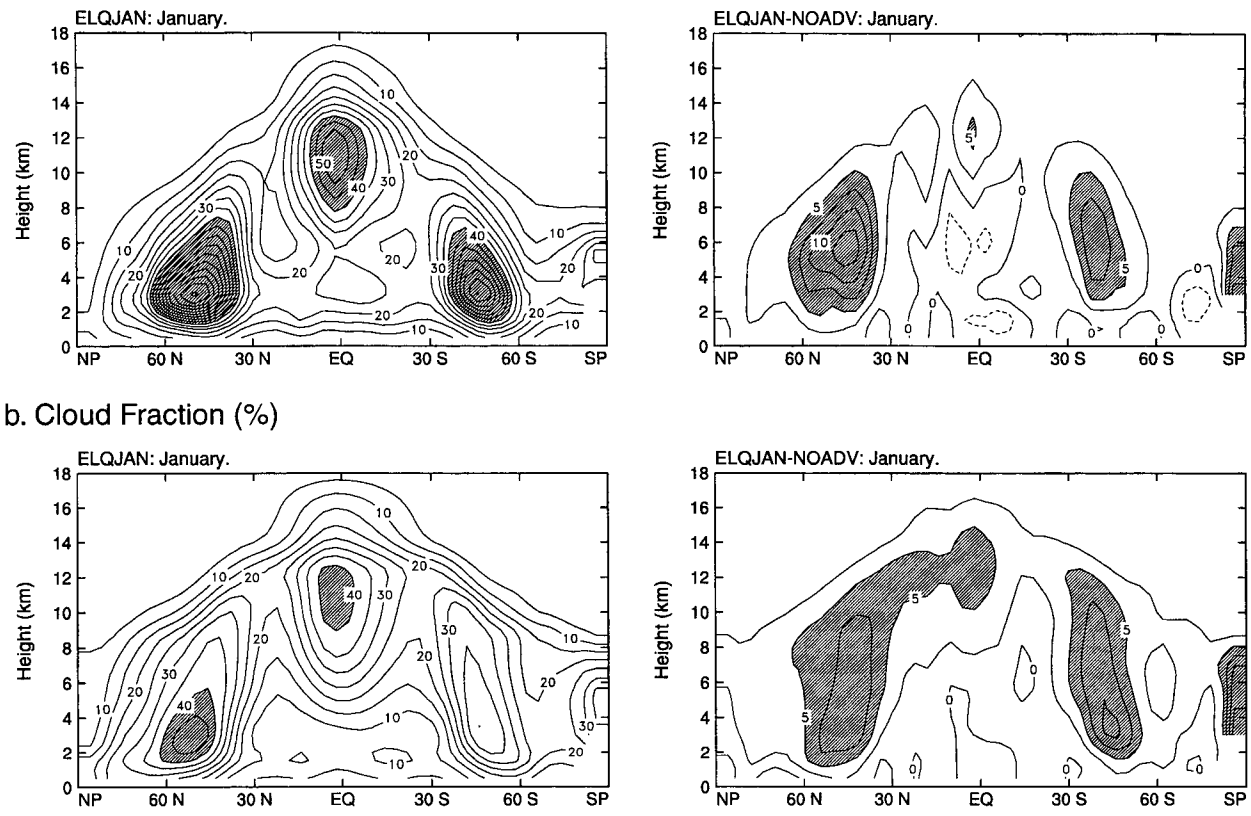

FIG. 4. Latitude–height cross sections of (a) the sum of the zonally averaged cloud water, cloud ice, and snow mixing ratios simulated by ELQJAN (left panel) and its difference between ELQJAN and NOADV (right panel), and (b) the zonally averaged cloud fraction simulated by ELQJAN (left panel), and its difference between ELQJAN and NOADV (right panel). In (a) contour intervals are every 5×10^{-6} kg kg^{-1} in the left panel and every 2.5×10^{-6} kg kg^{-1} in the right panel. Heavy shading corresponds to values greater than 40×10^{-6} kg kg^{-1} in the left panel and greater than 5×10^{-6} kg kg^{-1} in the right panel. In (b) contour intervals are every 5% in the left panel and every 2.5% in the right panel. Heavy shading corresponds to values greater than 40% in the left panel. Heavy shading corresponds to values greater than 5% in the right panel.

and snow; water vapor is, of course, advected as usual. We know that, at sufficiently high resolution, advection of condensed water will become important. An additional motivation for advection of the four condensed water species is to ensure conservation of the total water mass to machine precision. If the mass of dry air is spatially redistributed by the winds and the mixing ratios of condensed water are not correspondingly advected, then the mass of condensed water changes fictitiously. Because the PBL depth is variable in space and time and is the lowest layer of the model (Suarez et al. 1983), mass is also exchanged between the PBL and the layers above by turbulent entrainment and cumulus convection. Since the PBL is the lowest layer of the model, as it deepens and shoals, the layers above are pushed and pulled like the bellows of an accordion, implying mass exchange between these layers even if there is no "true" vertical motion. This process appears as a kind of "virtual advection." However, it is important to recall (see Part I) that, at present, the cloud microphysics parameterization is not applied to the PBL.

As discussed in Part I, the condensed water variables of the GCM are advected with a fourth-order horizontal advection scheme and a second-order vertical advection scheme. No parameterized "physical" diffusion is applied to these variables. Although the horizontal advection scheme conserves the mass-weighted square of the advected quantity and so in that sense is nondiffusive, dispersion errors lead to production of negative condensed water mixing ratios. These are corrected using a global multiplicative hole filler (Rood 1987). The advection scheme and hole filler acting together do produce some computational diffusion of the condensed water variables.

To highlight the impact of advection on the simulated moisture variables, Fig. 1 shows the latitude height cross sections of the zonally averaged differences between CW, CI, RW, and RI as simulated by ELQJAN and NOADV. Advection of the four water

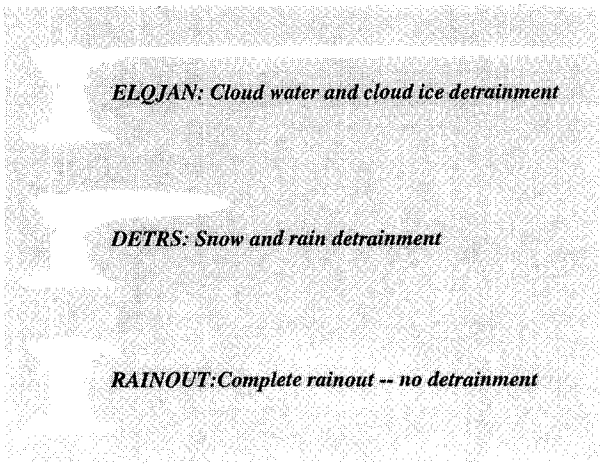

FIG. 5. Schematic diagram showing the difference in the size of the anvils between ELQJAN, DETRS, and RAINOUT.

species leads to a decrease in CW in the layer adjacent to the PBL and an increase in CW in the layers above, especially in the summer hemisphere. The associated decrease in RW remains confined along the equator, while RW increases outside the Tropics. In contrast, CI and RI undergo the largest increase in the middle latitudes in both hemispheres, at about 10 km and 6 km, respectively. The globally averaged increase in CW, RW, CI, and RI are equal to 0.2%, 6.3%, 5.3%, and 10.4%.

We looked in greater detail at the regional variations in CI and RI between ELQJAN and NOADV at the pressure levels at which advection leads to a maximum increase in their mixing ratios, as seen in Fig. 1. Figure 2 shows maps of CI at 200 mb, as simulated by ELQJAN and NOADV, and its difference ELQJAN minus NOADV. Figure 3 is as Fig. 2 but for RI located at 500 mb. As seen in Fig. 2, CI at 200 mb is the largest over the tropical convective activity centers because of strong detrainment of cloud ice at the tops of cumulus towers (refer to Fig. 3 of Part I). Areas of CI greater than 20×10^{-6} kg kg^{-1} are located over the winter monsoon region across the Indian and western Pacific Oceans, the equatorial Pacific Ocean, and southern Africa. At 500 mb, RI is the largest over the major storm track regions over the North Pacific and North Atlantic Oceans, as well as across the Southern Ocean, due to autoconversion of cloud ice to snow and collection of supercooled cloud water and cloud ice to form snow. Figures 2 and 3 are in accordance with the latitude–height cross sections of CI and RI described in Part I (refer to Figs. 7, 8). The map of the difference in CI between ELQJAN and NOADV indicates that advection generally produces a decrease in CI over areas of maximum CI production as simulated by NOADV whereas it increases in the vicinity of these maxima, as seen over the winter monsoon region, southern Africa, and the South Pacific convergence zone. Horizontal advection in effect diffuses CI over areas of major production sources, hence reducing its local maxima, as seen in Fig. 2. This effect is not as clearly seen in Fig. 3, probably because snow starts to fall as soon as it forms. On the other hand, the transport of RI by the horizontal flow is clearly evident, especially over the Southern Ocean. In general, advection has the tendency to increase the amount of CW, CI, RW, and RI by initiating cloud microphysical processes over areas where they would not occur otherwise. As seen in Fig. 1, this is not true for CW in the layer adjacent to the PBL because "virtual advection" carries CW inside the PBL, as explained above. As explained in Part I, CW is then forced to precipitate since cloud microphysical processes are not allowed to take place in the PBL.

Advection increases the cloud fraction C. In Fig. 4, the top panel shows latitude–height cross sections of the sum, CW + CI + RI, simulated with ELQJAN and its difference ELQJAN minus NOADV. It is CW + CI + RI that determines the distribution of clouds, as explained in Part II. The bottom panel of Fig. 4 shows the increase in C due to advection. Extratropical middle-level clouds are shown to increase the most, which is in accordance with the increase in CW + CI + RI that is observed in both hemispheres. A 5% increase in tropical high-level clouds also occurs. Advection increases the globally averaged cloud amount by 6.6%, with increases in high-, middle-, and low-level cloudiness of 8.5%, 4.6%, and 1.9%, respectively.[1] Advection increases C because, without it, the only processes that can allow cloud-free grid points to become cloudy are advection of vapor and potential temperature and cumulus detrainment. In ELQJAN, cloud-free grid points may also become overcast through advection of cloud water, cloud ice, or snow. The increase in C seen at 50°N and 50°S in Fig. 4 may be exaggerated due to the fact that our cloud microphysics parameterization does not include fractional cloudiness at this time. At present, C is set equal to 1 when CW + CI + RI is greater than 10^{-5} kg kg^{-1}. In summary, advection of condensed water has noticeable (but not dramatic) effects on the distribution of cloudiness even with the present coarse-resolution model. It will certainly become more important in future GCMs with higher resolution. Differences in the various components of the planetary radiation budget between NOADV and ELQJAN remain small, but could become significant when using increased spatial resolution. The increase in C between ELQJAN and NOADV leads to a decrease in the OLR of 4 W m^{-2}, whereas α increases by 0.8%.

[1] As in Part II, high- and low-level clouds are defined as clouds with cloud-top pressures less than 440 mb and greater than 680 mb, respectively.

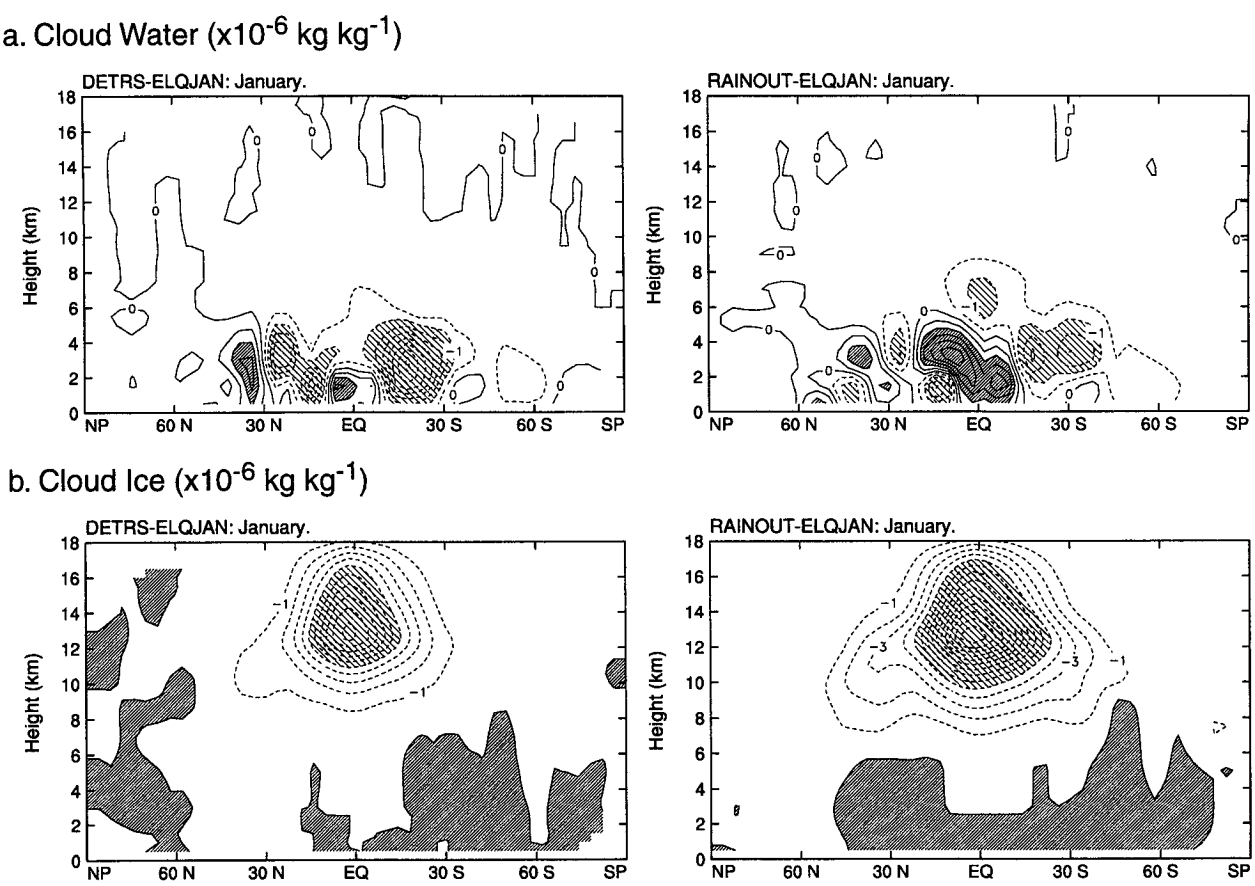

FIG. 6. Latitude–height cross sections of the zonally averaged differences in (a) the cloud water and (b) cloud ice mixing ratios between DETRS and ELQJAN (left panels) and between RAINOUT and ELQJAN (right panels). In (a) contour intervals are every 0.5×10^{-6} kg kg^{-1}. Light shading corresponds to values less than -1×10^{-6} kg kg^{-1}, and heavy shading corresponds to values greater than 1×10^{-6} kg kg^{-1}. In (b) contour intervals are every 1×10^{-6} kg kg^{-1}. Light shading corresponds to values less than -5×10^{-6} kg kg^{-1}. Heavy shading corresponds to values greater than 0.

4. Cumulus detrainment

Cumulus detrainment produces stratiform clouds, including persistent anvils and cirrus (Randall 1989). At present, some GCM microphysics parameterizations (Del Genio 1989; Ose 1993; Part I) supply detrained condensed water as a source for the stratiform cloud water and cloud ice. This choice is not unique, however, and it seems reasonable to consider the possibility that some fraction of the detrained condensed water may be supplied directly in the form of rain or snow. With this in mind, we designed the experiment referred to as DETRS. In addition, the experiment RAINOUT investigates an extreme assumption in which there is no direct coupling between cumulus convection and stratiform cloudiness.

The differences among DETRS, RAINOUT, and ELQJAN are illustrated in Fig. 5. In ELQJAN, as in Parts I and II, cloud water and cloud ice detrained at the tops of cumulus towers are used as sources of stratiform cloud water and cloud ice, respectively. This link between the cumulus and stratiform clouds allows the simulation of long-lived extended anvils, since cloud water droplets and cloud ice crystals remain suspended in the atmosphere until they become large enough to fall in the form of rain and snow. In DETRS, detrainment of cloud water and cloud ice is used as a source for rain and snow, rather than cloud water and cloud ice. The cloud optical effects of rain are neglected, as described in Part II. DETRS thus leads to a decrease in the anvil size, as sketched in Fig. 5. Although the optical properties of snow are considered in the model, stratiform anvils do not spread as widely in DETRS as in ELQJAN since snow starts to fall as soon as it forms, hence further reducing the horizontal fractional area covered by anvils.

The RAINOUT experiment eliminates the direct coupling between cumulus and stratiform clouds, and so further reduces the area covered by anvils, as shown in Fig. 5. In this extreme scenario, cloud water and cloud ice formed at the tops of cumulus towers are

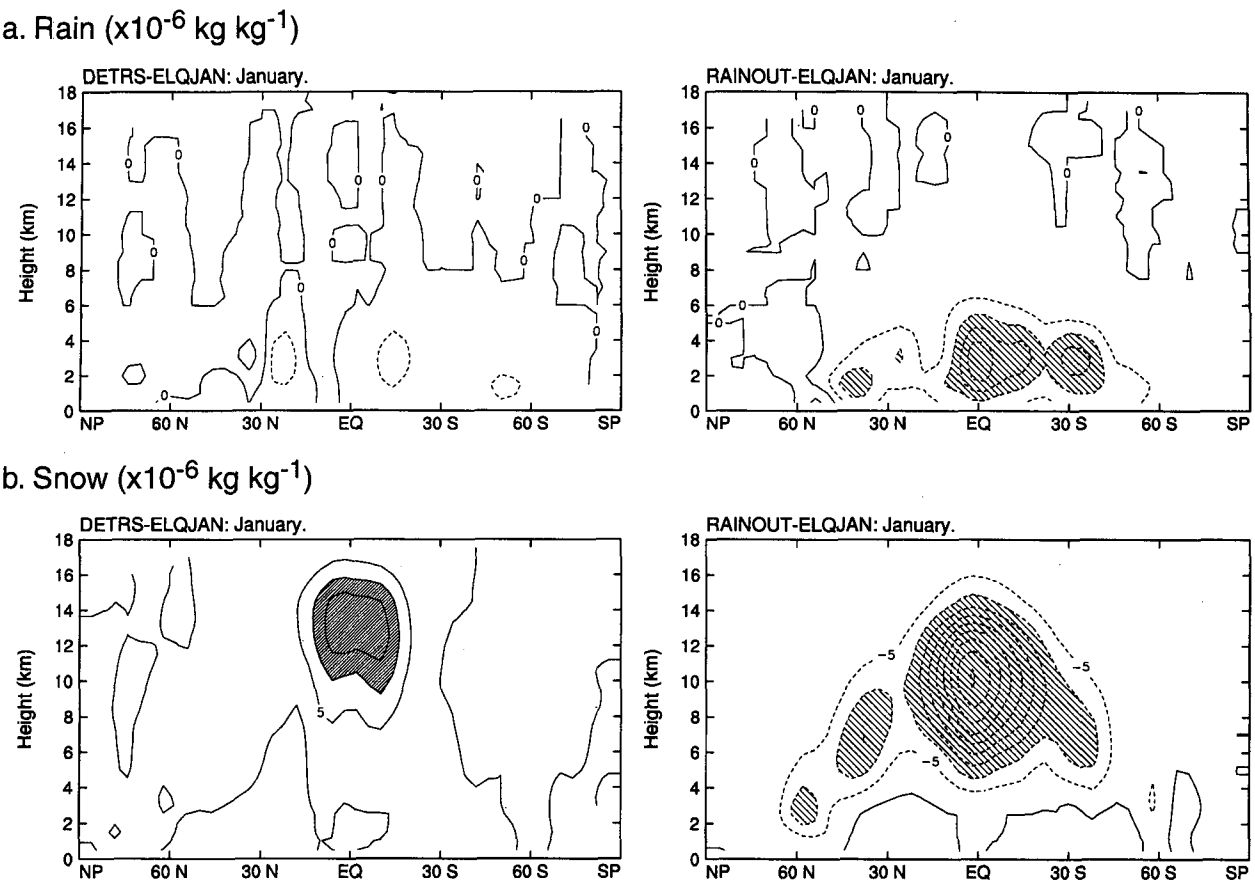

FIG. 7. Latitude–height cross sections of the zonally averaged differences in (a) the rain and (b) snow mixing ratios between DETRS and ELQJAN (left panels) and between RAINOUT and ELQJAN (right panels). In (a) contour intervals are every 0.5×10^{-6} kg kg^{-1}. Light shading corresponds to values less than -1×10^{-6} kg kg^{-1}. In (b) contour intervals are every 5×10^{-6} kg kg^{-1}. Light shading corresponds to values less than -10×10^{-6} kg kg^{-1}, and heavy shading corresponds to values greater than 10×10^{-6} kg kg^{-1}.

immediately removed from the atmosphere in the form of precipitation of rain and snow. Radiatively active anvil clouds can still be produced by supersaturation resulting from an accumulation of detrained vapor, but their lifetimes are shorter than those of the anvils formed in ELQJAN and DETRS.

Interactions between the bulk cloud microphysics parameterization and cumulus convection, and the rates of detrainment of cloud water and cloud ice, are discussed in Part I. As shown in Part I (refer to Fig. 3), the cumulus parameterization is more efficient at detraining cloud ice than cloud water. This affects the partitioning between the stratiform cloud water and cloud ice.

The latitude–height distributions of CW, CI, RW, and RI are discussed in detail in Part I, where it was reported that, in the model results, snow is the most abundant water species after water vapor. Figure 6 shows the latitude–height cross sections of the zonally averaged differences in CW and CI between DETRS and ELQJAN and between RAINOUT and ELQJAN. Figure 7 is like Fig. 6 but for the differences in RW and RI. To detrain cloud water and cloud ice in the form of rain and snow or to immediately remove detrained cloud water and cloud ice in the form of precipitation yields, of course, a decrease in the amount of CW and CI suspended in the atmosphere. Because detrainment of cloud ice is stronger than that of cloud water, the change in CI and then RI is then more dramatic than those in CW and RW; CW actually increases along the equator and at about 30°N. This effect results because evaporation increases, hence leading to enhanced supersaturation conditions at low altitudes. A difference map of the relative humidity at 850 mb and 700 mb between RAINOUT and ELQJAN would show that the relative humidity increases over some tropical areas, especially over the monsoon region. In DETRS, RW decreases slightly even though cumulus detrainment of cloud water acts directly as a source of rain. This occurs because, by assumption (refer to Part I), larger rain amounts have greater fall speeds and so are removed faster. In contrast, RI increases in DETRS relative to ELQJAN because cumulus detrainment of cloud ice is strong and the fall speed of snow is smaller

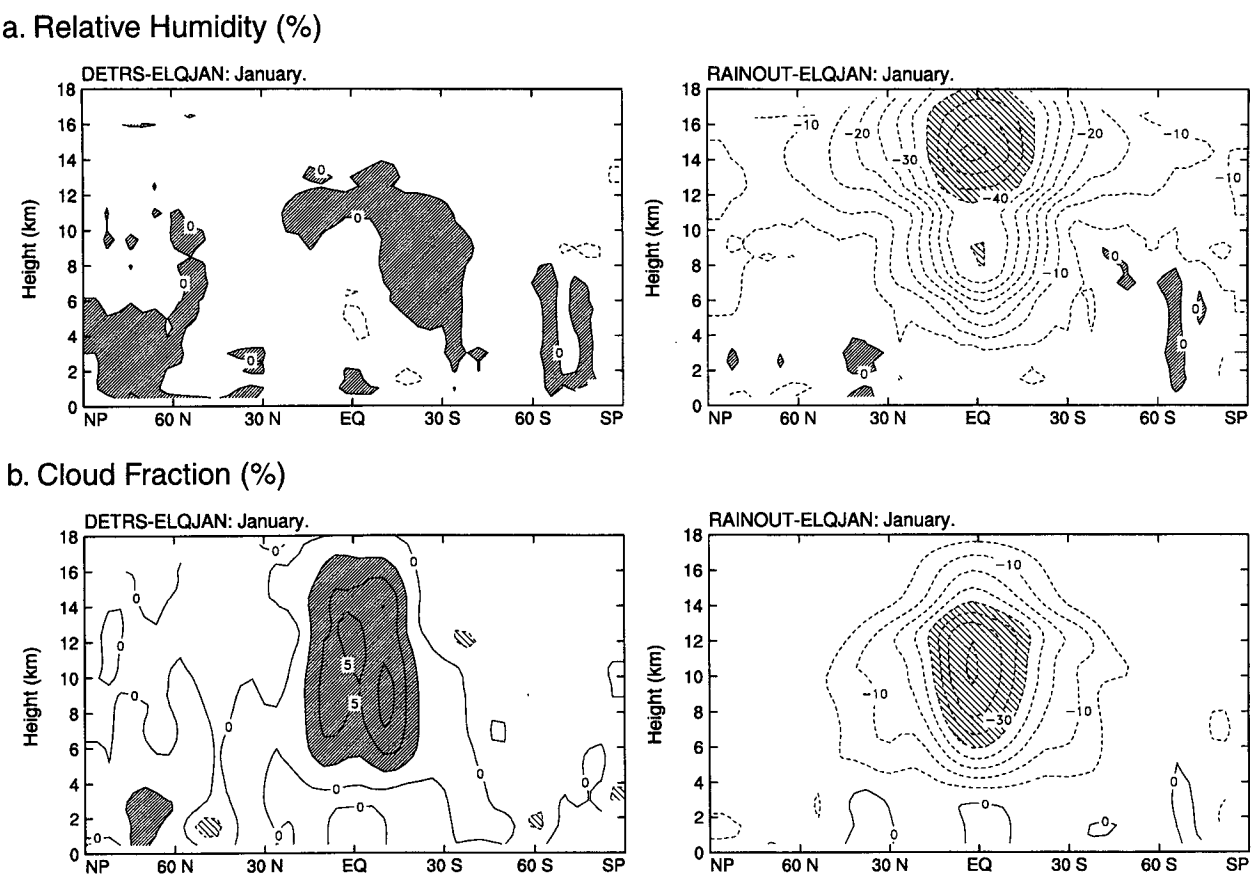

FIG. 8. Latitude–height cross sections of the zonally averaged differences in (a) the relative humidity and (b) the cloud fraction between DETRS and ELQJAN (left panels) and between RAINOUT and ELQJAN (right panels). Units are percent. In (a) contour intervals are every 5%. Light shading corresponds to values less than −40%. Heavy shading corresponds to values greater than 0. In (b) contour intervals are every 2.5% in the left panel and every 5% in the right panel. Light shading corresponds to values less than −25%, and heavy shading corresponds to values greater than 2.5%.

than that of rain. RAINOUT leads to an overall drying of the atmosphere. On a global average, the water vapor path is reduced from 23.3 to 20.1 kg m^{-2}, hence significantly slowing down the occurrence of condensation and deposition processes. As a result, RAINOUT yields large reductions in RW and RI.

The differences in relative humidity and cloud amount between DETRS and ELQJAN and between RAINOUT and ELQJAN are plotted in Fig. 8. The decrease in the amount of water condensate suspended in the atmosphere leads to a very significant decrease in the relative humidity, especially in the tropical upper troposphere in RAINOUT. This is because the source of detrained cloud water and cloud ice is the strongest in the Tropics and has been cut off in RAINOUT. The effect is much weaker in DETRS since snow and rain are still detrained.

As shown in Fig. 8, middle- and high-level cloudiness increase in DETRS, especially along the equator. This increase in middle-level cloudiness between DETRS and ELQJAN occurs because, in contrast to cloud ice, which remains suspended in the atmosphere, snow starts to fall as soon as it forms, hence leading to the occurrence of clouds at levels lower than those where ice clouds most often form in ELQJAN. In contrast, RAINOUT yields strong decreases in both middle- and high-level clouds in the Tropics because CW + CI + RI is strongly reduced, as shown in Figs. 6 and 7. In DETRS and RAINOUT, the global averages of CW + CI + RI are 0.202 kg m^{-2} and 0.141 kg m^{-2}, respectively, versus 0.198 kg m^{-2} in ELQJAN. High cloud amount decreases by 1% in DETRS and 20% in RAINOUT. In DETRS, the much weaker decrease in high cloud amount occurs because the source of cloud ice is replaced by a source of snow so that, as a whole, almost as much condensed water is available for clouds to form as in ELQJAN. A more drastic response is obtained in RAINOUT, in which the source of detrained condensed water for clouds is completely cut off. In addition, middle-level cloud amount decreases by 7.7% in RAINOUT.

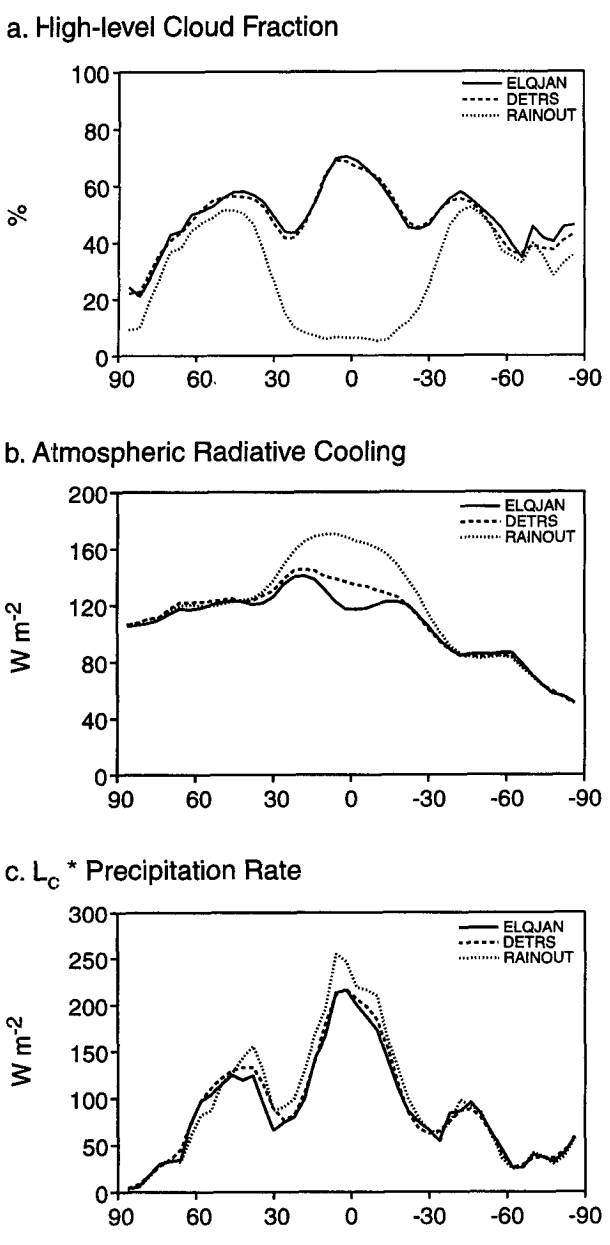

FIG. 9. Zonally averaged distributions of (a) the high-level cloud fraction in percent, (b) atmospheric radiative cooling in W m^{-2}, and (c) precipitation rate times the latent heat of condensation in W m^{-2} simulated by ELQJAN (solid line), DETRS (dashed line), and RAINOUT (dotted line).

ELQJAN, DETRS, and RAINOUT provide examples of the negative "global radiative–convective feedback" reported by Fowler and Randall (1994). This feedback works as follows: On a global scale, increased convective activity yields the formation of a thicker upper-tropospheric cloud shield, which leads to reduced atmospheric radiative cooling (ARC) and a more statically stable atmosphere. Here, the ARC is defined as the difference between the net radiation budgets at the earth's surface and the top of the atmosphere. Cumulus convection is then suppressed and the total precipitation rate decreases. The system equilibrates when the ARC and the latent heating are in balance. To illustrate this concept as it applies to these numerical experiments, Fig. 9 shows the zonally averaged distributions of the high cloud amount, ARC, and precipitation rate simulated by ELQJAN, DETRS, and RAINOUT. The precipitation rate is expressed as a latent heat flux by multiplying its value by the latent heat of condensation. On a global average, the ARC is balanced by the sum of the latent heat flux and sensible heat flux. Because, on a global average, the sensible heat flux is much smaller than the latent heat flux, variations in the magnitude of the ARC are primarily balanced by changes in the net latent heating, that is, the precipitation rate.

The decrease in high cloud amount between ELQJAN, DETRS, and RAINOUT yields an increased ARC and latent heat flux, primarily between 30°N and 30°S. The largest difference occurs, of course, in RAINOUT. The increased precipitation rate occurs in the Tropics and in middle latitudes in the winter hemisphere. In DETRS and RAINOUT, the cumulus precipitation rates are 1.90 mm day^{-1} and 1.84 mm day^{-1}, respectively, versus 1.72 mm day^{-1} in ELQJAN. RAINOUT leads to a significant increase in the large-scale precipitation rate from 1.96 mm day^{-1} in ELQJAN to 2.32 mm day^{-1}. The change in cloudiness has a substantial impact on the top-of-the-atmosphere planetary radiation budget simulated by RAINOUT and a lesser impact on that simulated by DETRS. In DETRS and RAINOUT, the OLR increases by 6.7 W m^{-2} and 22.4 W m^{-2}, respectively, whereas α decreases by 1.8% and 3.7%, respectively. Further discussion is given in section 9.

In summary, the use of detrained condensate as a source of rain and snow in DETRS, instead of a source of cloud water and cloud ice as in ELQJAN, has little impact upon the hydrologic cycle, planetary radiation balance, and cloudiness simulated with the CSU CGM. This actually is reassuring because we do not want our results to be too strongly influenced by the details of the coupling between convective and large-scale clouds.

In contrast, RAINOUT produces substantial differences in the simulated climate. The drying of the atmosphere leads to a reduction in the amount of water condensate available to form clouds, in particular high-level clouds, hence leading to a warmer OLR and decreased α. Precipitation rates increase, especially in the Tropics. The results of RAINOUT illustrate the importance of the cumulus detrainment of condensed water for the hydrologic cycle and the earth's radiation budget.

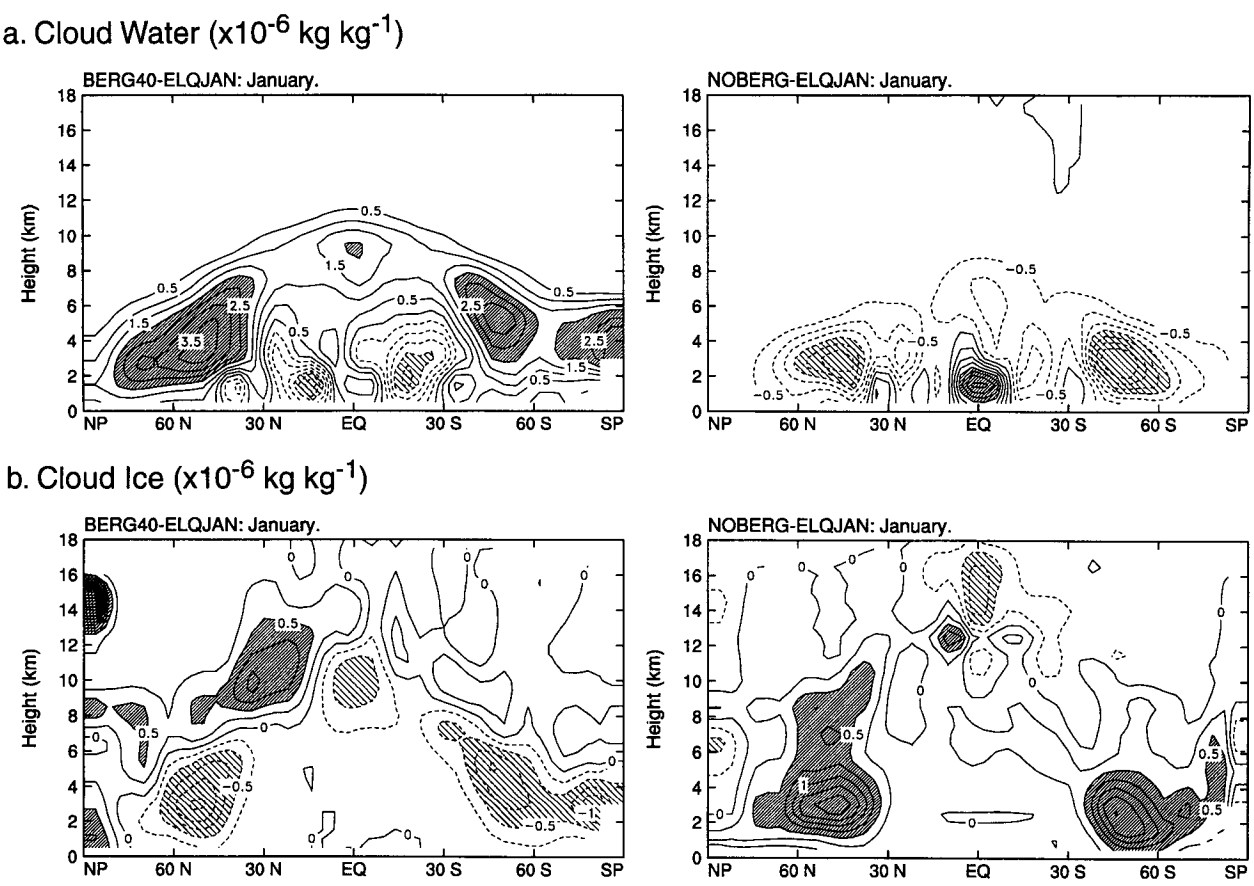

FIG. 10. Latitude–height cross sections of the zonally averaged differences in (a) the cloud water and (b) cloud ice mixing ratios between BERG40 and ELQJAN (left panels) and between NOBERG and ELQJAN (right panels). In (a) contour intervals are every 0.5×10^{-6} kg kg^{-1}. Light shading corresponds to values less than -2×10^{-6} kg kg^{-1}, and heavy shading corresponds to values greater than 2×10^{-6} kg kg^{-1}. In (b) contour intervals are every 0.25×10^{-6} kg kg^{-1}. Light shading corresponds to values less than -0.5×10^{-6} kg kg^{-1}, and heavy shading corresponds to values greater than 0.5×10^{-6} kg kg^{-1}.

5. Mixed-phase clouds

The threshold temperature dividing mixed-phase clouds from ice clouds is not well known but may be an important modulator of the climate sensitivity in climate change experiments. Senior and Mitchell (1993) show that, in the case of a doubling of the atmospheric CO_2, the increasing fraction of cloud water relative to cloud ice leads to a negative feedback, which becomes even more negative when cloud optical properties are computed as functions of the cloud water and cloud ice paths.

In this section, we compare the climates simulated by the CSU CGM when mixed-phase clouds are allowed to form in the temperature range $-20°C \leq T < 0°C$ (ELQJAN) and $-40°C \leq T < 0°C$ (BERG40) and when no mixed-phase clouds are allowed to form (NOBERG). We define mixed-phase clouds as those in which supercooled cloud water and cloud ice coexist; that is, where the Bergeron–Findeisen process (PBERG) is active (refer to section 2b and appendix A of Part I).

In ELQJAN, cloud ice and supercooled cloud water are allowed to coexist in the temperature range $-20°C \leq T < 0°C$. At temperatures lower than $-20°C$, supercooled cloud water is assumed to freeze instantaneously to become cloud ice. At temperatures higher than 0°C, cloud ice is assumed to melt instantaneously to become cloud water. As the temperature range over which mixed-phase clouds are allowed to occur widens, the amount of supercooled cloud water increases at the expense of cloud ice. The mixed-phase cloud amounts strongly influences the top-of-the-atmosphere longwave and shortwave radiation budgets since the cloud optical properties depend on the partitioning between cloud water and cloud ice. We compute the cloud optical depth τ, the infrared emissivity ϵ, single scattering albedo ω_0, and asymmetry factor g of mixed-phase clouds using Eqs. (2), (3), (4), and (5) of Part II. In ELQJAN, BERG40, and NOBERG, the cloud optical properties of PBL clouds follow the formulation of Harshvardhan et al. (1989; also described in Part II), since the cloud mi-

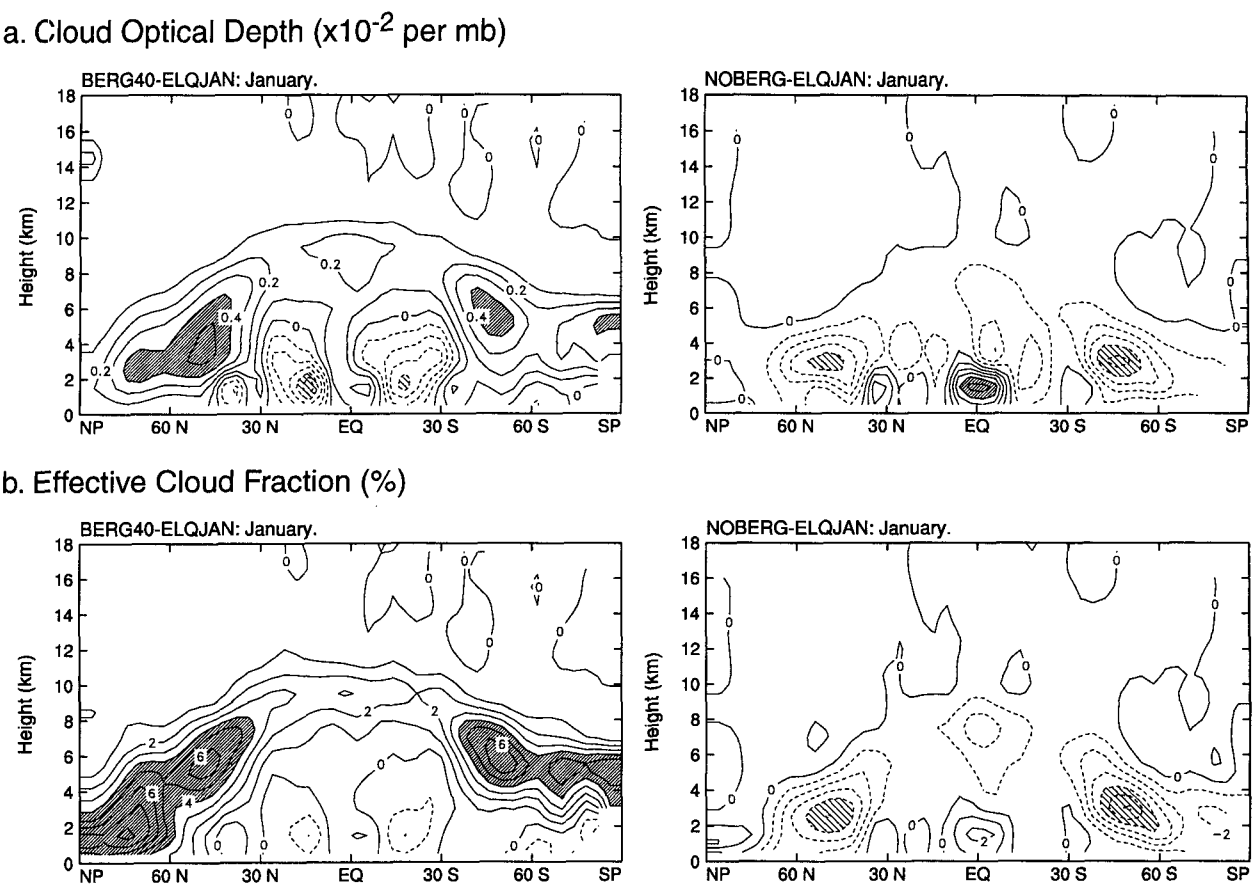

FIG. 11. Latitude–height cross sections of the zonally averaged differences in (a) the cloud optical depth and (b) effective cloud fraction between BERG40 and ELQJAN (left panels) and between NOBERG and ELQJAN (right panels). In (a) contour intervals are every 0.1 $\times 10^{-2}$ per mb. Light shading corresponds to values less than -0.4×10^{-2} per mb, and heavy shading corresponds to values greater than 0.4×10^{-2} per mb. In (b) contour intervals are every 1%. Light shading corresponds to values less than −4%, and heavy shading corresponds to values greater than 4%.

crophysics parameterization is not currently applied to the PBL.

Figure 10 shows the latitude–height cross sections of the zonally averaged differences of CW and CI between BERG40 and ELQJAN and between NOBERG and ELQJAN. In BERG40, supercooled cloud water increases at the expense of cloud ice between −40°C and −20°C. In NOBERG, the reverse happens, and cloud ice increases at the expense of supercooled cloud water. It is interesting to note that, in BERG40, the increase in CW (on a global average, +0.006 kg m^{-2}) does not even approximately compensate the decrease in CI (−0.001 kg m^{-2}). This result can be traced to our assumption that supercooled cloud water may be converted to snow with the same autoconversion threshold as that used to convert cloud water to rain (q_{c0} = 0.25 g kg^{-1}). In contrast, the autoconversion threshold for cloud ice to snow is 0.01 g kg^{-1}, which forces removal of cloud ice from the atmosphere faster than supercooled cloud water. A closer compensation is observed in NOBERG, for which the decrease in CW is −0.004 kg m^{-2}, while the increase in CI is +0.002 kg m^{-2}.

The sum CW + CI + RI, which determines the occurrence of clouds and their cloud optical properties, varies little among the three experiments. CW + CI + RI is 0.198 kg m^{-2} in ELQJAN versus 0.212 kg m^{-2} in BERG40 and 0.196 kg m^{-2} in NOBERG. This change in CW + CI + RI yields changes in the globally averaged cloud fraction of +1.4% between BERG40 and ELQJAN and −0.6% between NOBERG and ELQJAN. Hence, the changes in the cloud optical depth and cloud infrared emissivity among the three experiments are essentially due to the change in partitioning between the amounts of cloud water and cloud ice.

Figure 11 shows the latitude–height cross sections of the zonally averaged differences in τ and C_{ef} between BERG40 and ELQJAN and between NOBERG and ELQJAN. In BERG40, the increased supercooled cloud water leads to increased values of τ and C_{ef} for middle- and high-level clouds. The reasons are 1) τ is

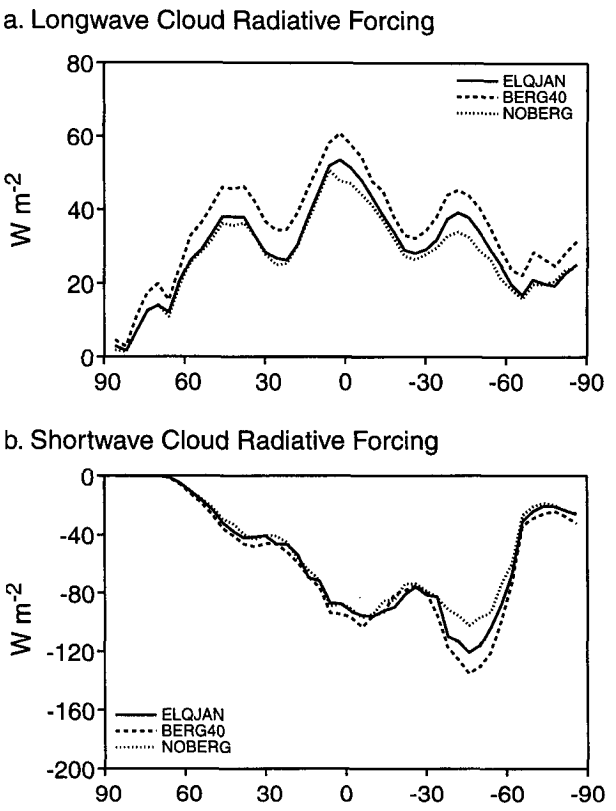

FIG. 12. Zonally averaged distributions of the top-of-the-atmosphere (a) longwave cloud radiative forcing and (b) shortwave cloud radiative forcing simulated by ELQJAN (solid line), BERG40 (dashed line), and (c) NOBERG (dotted line). Units are W m^{-2}.

proportional to the cloud water path, which is greater in BERG40 than in ELQJAN, and 2) τ is inversely proportional to the effective radius, which is smaller for cloud water (10 μm) than for cloud ice (30μm). Referring to Eq. (2) of Part II, we see that larger cloud optical depths yield larger cloud infrared emissivities and hence greater effective cloud cover, providing that the cloud amount remains constant. The results of NOBERG show a decrease in τ and C_{ef} for middle- and high-level clouds in the Tropics and middle latitudes. This decrease occurs because the increase in cloud ice is not sufficient to compensate the decrease in cloud water, and the effective radius for cloud ice is larger than that for cloud water.

Finally, Fig. 12 shows the distributions of the zonally averaged longwave (LWCRF) and shortwave (SWCRF) cloud radiative forcings obtained in the three experiments. When compared to ELQJAN, BERG40 leads to increased LWCRF and SWCRF, whereas NOBERG leads to decreased cloud forcing at all latitudes. These variations are in accordance with the change in the cloud optical properties described above. Optically thicker (thinner) clouds increase (decrease) the amount of shortwave solar radiation reflected at cloud tops, hence enhancing the radiative effect of clouds at short wavelengths. In addition, increasing (decreasing) effective cloud fraction yields a decreased (increased) outgoing infrared radiation, hence enhancing (decreasing) the longwave cloud radiative forcing. On a global average, and relative to ELQJAN, the LWCRF changes by +6.4 W m^{-2} in BERG40 and −2.0 W m^{-2} in NOBERG, and the SWCRF changes by −4.2 W m^{-2} in BERG40 and +3.9 W m^{-2} in NOBERG.

It is interesting to note that although we changed the width of the temperature window over which PBERG is active by the same increment (in the two experiments, we increased it by 20°C in BERG40 and decreased it by 20°C in NOBERG), the response is much stronger in BERG40 than in NOBERG. For instance, the increase in supercooled cloud water in BERG40 is greater than the increase in cloud ice in NOBERG. Also, the absolute change in the cloud radiative forcing between BERG40 and ELQJAN is greater than that between NOBERG and ELQJAN. The difference in strength of the response in the two experiments is because the microphysics and optical properties of water clouds and ice clouds are parameterized differently. The thresholds for autoconversion of supercooled cloud water and cloud ice to snow are different, hence allowing supercooled cloud water to remain suspended in the atmosphere longer than cloud ice. The effective radius for cloud water is smaller than that for cloud ice, which leads to cloud optical depths and infrared emissivities that are greater in BERG40 than in NOBERG.

6. Fall speeds

In ELQJAN, the mass-weighted fall speeds of rain and snow are parameterized following the experimental results of Gunn and Kinzer (1949) and Locatelli and Hobbs (1974), respectively. Both fall speeds depend on the slope of the size distributions for rain and snow, which follow Gunn and Marshall (1958). In FALLRS, we simply increase both fall speeds by a factor of 2 to evaluate the impact of fall speed on the removal of cloud water and cloud ice by autoconversion and collection processes.

Figure 13 shows the latitude–height cross sections of the zonally averaged tendencies of rain and snow due to precipitation, as simulated by ELQJAN, and their differences between FALLRS and ELQJAN. Negative values for the tendencies indicate areas of depletion of rain and snow. Areas of largest depletion of rain and snow coincide, of course, with areas of maximum rain and snow production, since the fall speeds of rain and snow are functions of the rain and snow mixing ratios. Therefore, and in accordance with the latitude–height cross sections of RW and RI shown in Fig. 7 of Part I, the depletion of rain due to precipitation is the largest at the 3-km level between 30°N and 30°S. The removal of snow due to precipitation is the strongest at

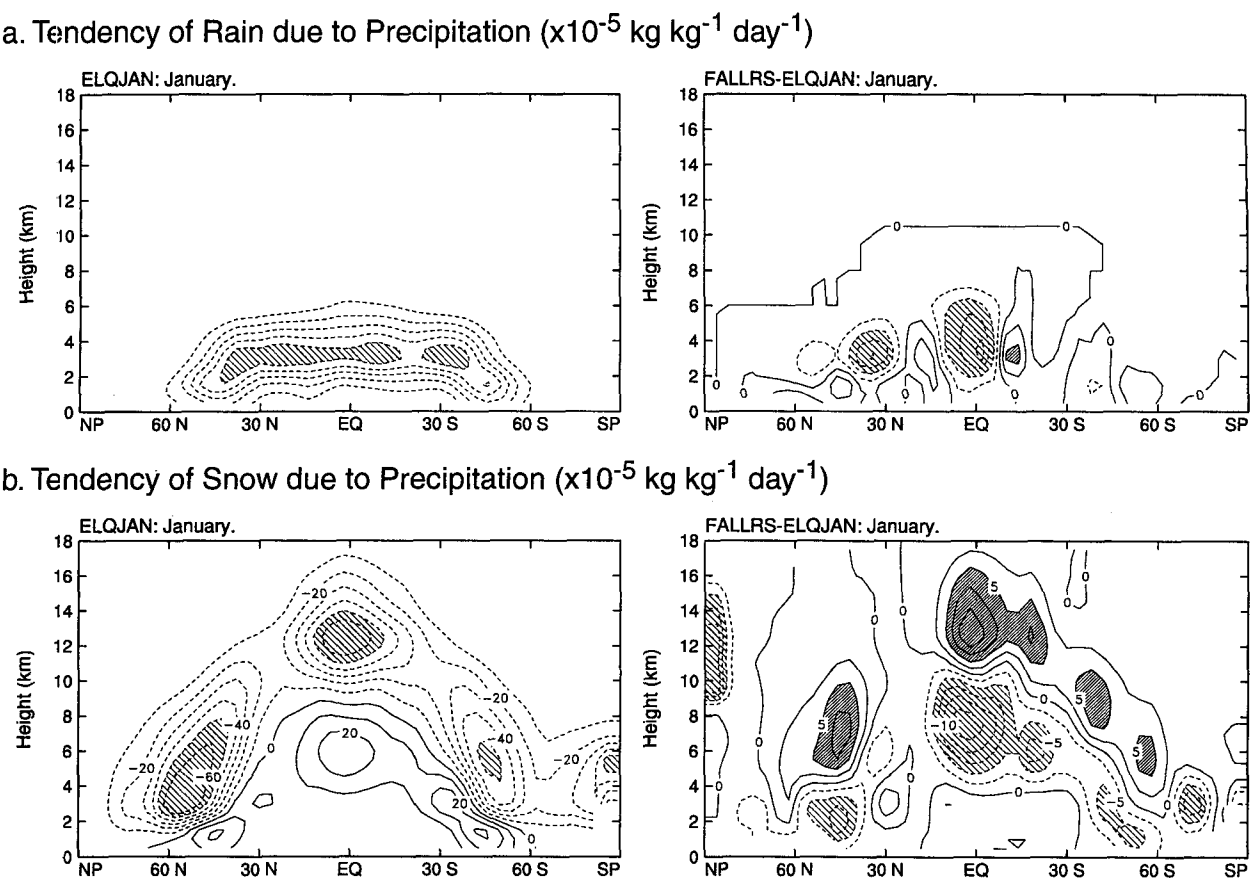

FIG. 13. Latitude–height cross sections of the zonally averaged (a) tendency of rain due to precipitation (left panel) simulated by ELQJAN and its difference between FALLRS and ELQJAN (right panel), and (b) tendency of snow due to precipitation simulated by ELQJAN (left panel) and its difference between FALLRS and ELQJAN (right panel). In the left panels, contour intervals are every 10×10^{-5} kg kg^{-1} day^{-1}. Light shading corresponds to values less than -50×10^{-5} kg kg^{-1} day^{-1}. In the right panels, contour intervals are every 2.5×10^{-5} kg kg^{-1} day^{-1}. Light shading corresponds to values less than -5×10^{-5} kg kg^{-1} day^{-1}, and heavy shading corresponds to values greater than 5×10^{-5} kg kg^{-1} day^{-1}.

about 12 km along the equator and at about 4 km around 60°N in the winter hemisphere. An accumulation of snow due to precipitation is found just above the freezing level where instantaneous melting of snow to form rain takes place. The right-hand panels of Fig. 13 show that increasing the fall speed of rain and snow does not systematically lead to an increase in the tendencies of rain and snow due to precipitation at all latitudes. Negative (positive) differences between FALLRS and ELQJAN correspond to increased (decreased) depletions of rain and snow from the free troposphere. Figure 13 indicates that doubling the fall speed of rain removes rain faster along the equator and at about 30°N. More interestingly, doubling the fall speed of snow yields snow to be removed slower at all altitudes at which the tendency of snow due to precipitation is maximum, whereas snow is removed faster in the layers where instantaneous melting of snow to rain occurs. The decrease in the tendencies of rain and snow between FALLRS and ELQJAN results because, in FALLRS, less rain and snow remain suspended in the atmosphere due to their increased fall speed.

The impact of increasing the fall speeds of rain and snow on CW, CI, RW, and RI is shown in Fig. 14. On a zonal average, CW increases at almost all latitudes. This occurs because less rain and snow are made available to collect cloud water, and especially because less snow is available to collect supercooled cloud water to form snow, as discussed in section 8. Evaporation of rain and snow in subsaturated layers, followed by condensation to form cloud water when the layer becomes supersaturated, is not as frequent a process as collection. Figure 14 shows that CI changes very little between ELQJAN and FALLRS. In FALLRS, the decrease in RW and RI at all latitudes results, of course, because of the faster depletion of rain and snow due to their increased fall speeds.

The impact of increasing the fall speeds of rain and snow on cloudiness and stratiform precipitation are displayed in Figs. 15 and 16, respectively. The change in

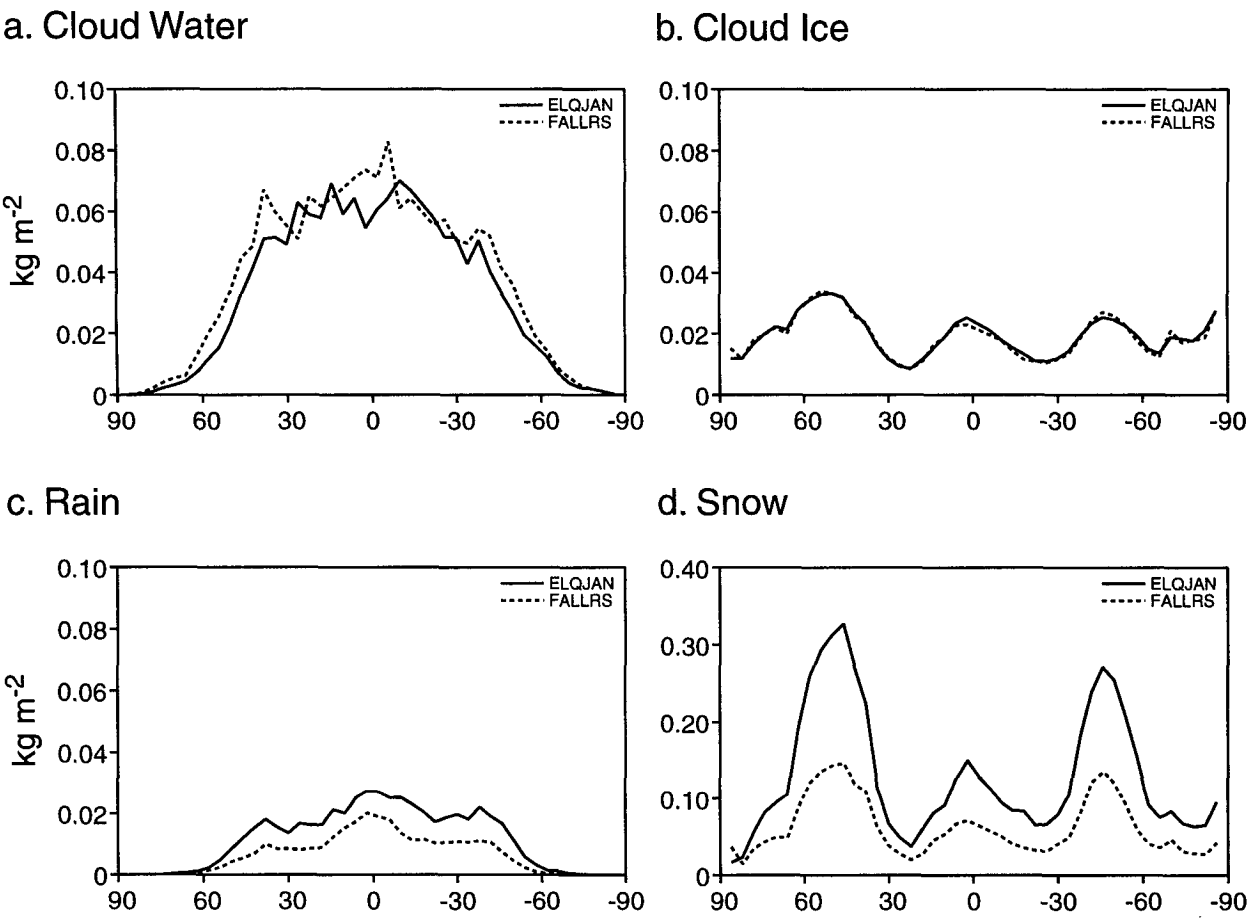

FIG. 14. Zonally averaged distributions of (a) the cloud water, (b) cloud ice, (c) rain, and (d) snow mixing ratios simulated by ELQJAN (solid line) and FALLRS (dashed line). Units are kg m^{-2}.

RW between FALLRS and ELQJAN has no direct effect on cloudiness since the optical effects of rain are neglected. The decrease in the total cloud fraction essentially results from a decrease in the amount of middle- and high-level clouds, although low-level clouds are also shown to decrease in the middle latitudes. On a global average, the 4.9% decrease in the total cloud fraction corresponds to a decrease of 6.1%, 4.9%, and 1.7% in the high-, middle-, and low-level cloud fractions, respectively. High-level clouds decrease at all latitudes, whereas middle-level clouds decrease mostly in the middle latitudes in both hemispheres. The latitude–height cross section of the zonally averaged difference in the total cloud fraction between FALLRS and ELQJAN (not shown) indicates that, as for the experiment NOADV, the cloud fraction decreases mainly in the middle latitudes of the winter hemisphere because of the strong decrease in RI. Figure 16 indicates that increasing the fall speed of rain and snow leads to an enhancement of the stratiform rain rate in the Tropics, while the stratiform snowfall rate varies little in the middle latitudes. On a global average, the rainfall rate increases by 8%, whereas snowfall increases only by 4.6%. This result is in accordance with the respective increase in the tendencies of rain and snow due to precipitation, as shown in Fig. 13. As for the tendency of rain, the increase in the Tropics also results from the melting of snow falling through layers above the melting level. Finally, the decrease in high-level clouds between FALLRS and ELQJAN yields a 2.7 W m^{-2} increase in OLR and a 0.22% decrease in α.

7. Autoconversion thresholds

Two of the most important parameters of our cloud microphysics parameterization are the thresholds for autoconversion of cloud water to rain (q_{c0}) and cloud ice to snow (q_{i0}). By definition, q_{c0} and q_{i0} are prescribed mixing ratios above which cloud water and cloud ice are converted to rain and snow, respectively, until their mixing ratios do not exceed q_{c0} and q_{i0}. In Parts I and II, q_{c0} was chosen so that the simulated vertically integrated cloud water was in reasonable

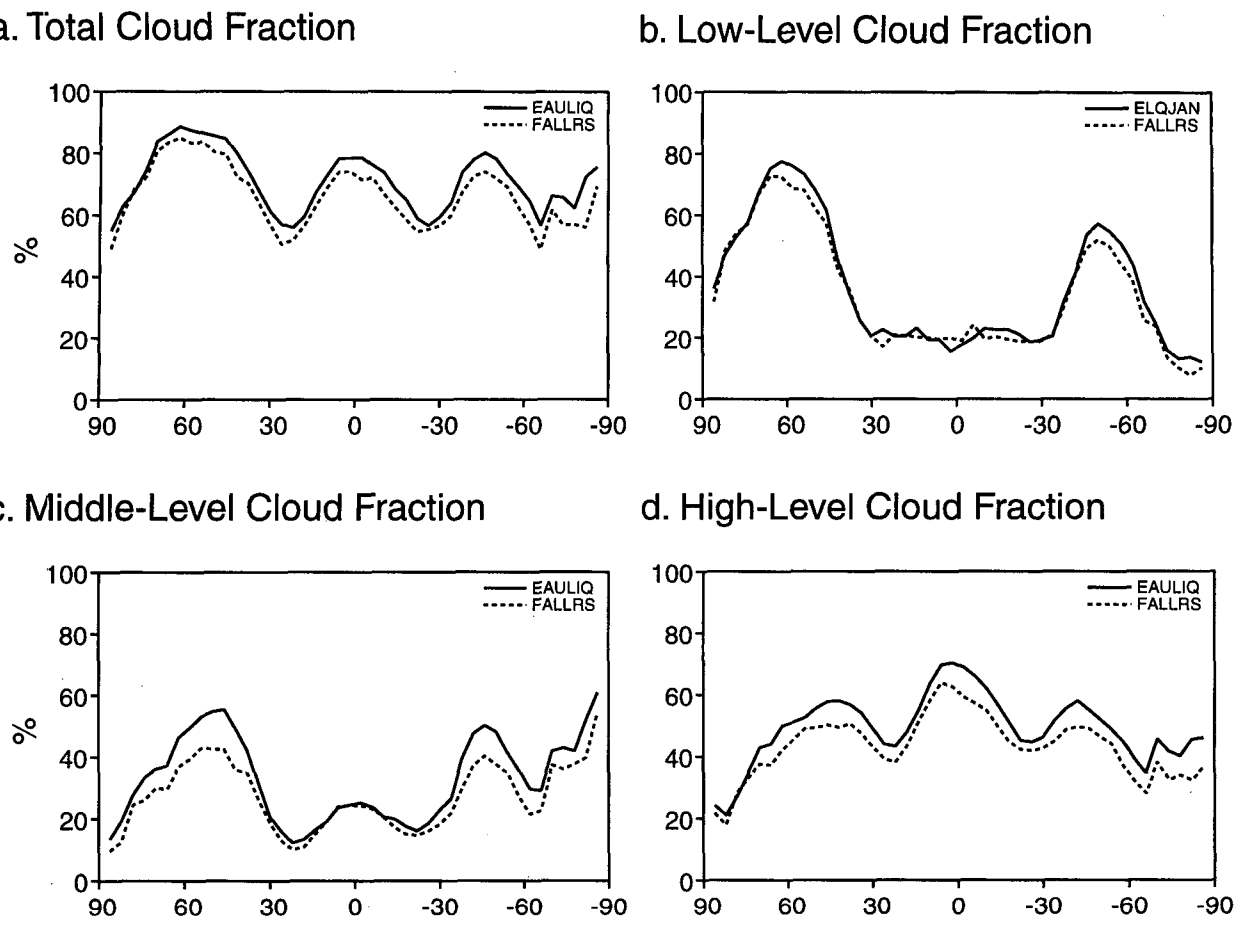

FIG. 15. Zonally averaged distributions of (a) the total cloud fraction, (b) low-level cloud fraction, (c) middle-level cloud fraction, and (d) high-level cloud fraction simulated by ELQJAN (solid line) and FALLRS (dashed line). Units are percent.

agreement with cloud water estimates derived from SSM/I microwave radiances (Greenwald et al. 1993); q_{i0}, which strongly influences the areal coverage of tropical anvils, was adjusted so that the simulated outgoing infrared radiation of convectively active regions was close to that observed by ERBE (Barkstrom and Smith 1986). Note that only these two numerical coefficients of our cloud microphysics parameterization were adjusted in this way and that their values are geographically and temporally constant. A discussion of the scale dependence of the cloud microphysical parameters can be found in Part I.

The appropriate choices for q_{c0} and q_{i0} are strongly dependent upon the spatial resolution of the GCM and on the model's parameterization of fractional cloudiness, or lack thereof. In the present model, each grid box is assumed to be either overcast or cloud free. Given this assumption, the condensed water is uniformly distributed over the whole grid box, and autoconversion thresholds have to be drastically reduced to prevent the formation of excessively widespread and thick cloud water and cloud ice shields.

In experiments QCW0 and QCI0, the impacts of increasing q_{c0} and q_{i0} are investigated separately. In QCW0, q_{c0} is increased from 0.25 g kg^{-1} to 0.7 g kg^{-1}, while in QCI0, q_{i0} is increased from 0.01 g kg^{-1} to 0.03 g kg^{-1}. The value used by Rutledge and Hobbs (1983, 1984) is 0.7 g kg^{-1} while q_{i0} was set equal to 0.1 g kg^{-1} by Lin et al. (1983).

Figure 17 shows maps of the vertically integrated cloud water path and cloud ice path simulated by ELQJAN, and maps of their differences between QCW0 and ELQJAN and between QCI0 and ELQJAN, respectively. Discussion of the geographical distributions of CW and CI may be found in Part I. Briefly, CW and CI are the largest over the tropical convectively active regions over land and oceans, as well as above the major storm track regions in the winter hemisphere. Cloud ice paths greater than 2×10^{-2} kg m^{-2} are also simulated across the Southern Ocean. The increases in CW and CI due to the increased autoconversion thresholds occur, of course, over areas of maximum CW and CI, that is, mainly over convectively active regions in the Tropics for CW and at high lati-

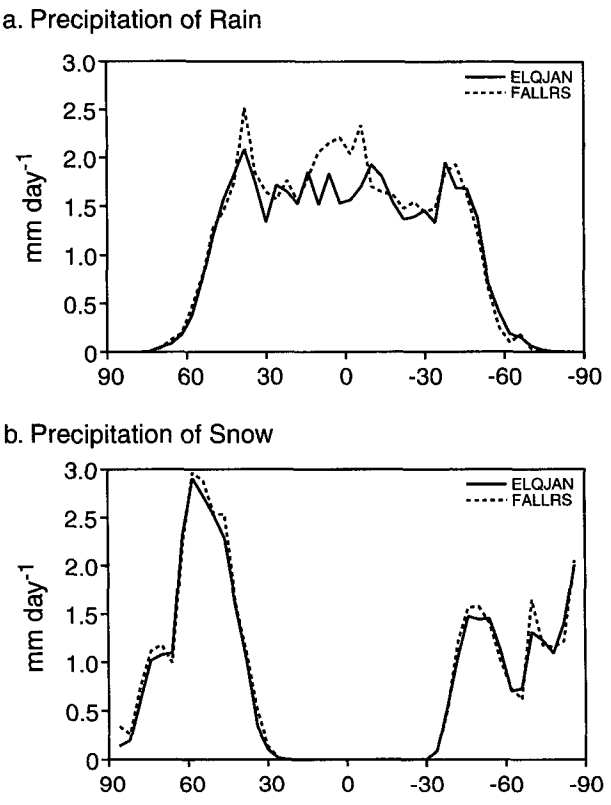

FIG. 16. Zonally averaged distributions of (a) the large-scale precipitation rate of rain and (b) large-scale precipitation rate of snow simulated by ELQJAN (solid line) and FALLRS (dashed line). Units are millimeters per day.

tudes in the winter hemisphere for CI. The prescribed increases in q_{c0} and q_{i0} lead to increases of 70.5% in CW and 63.2% in CI, respectively. This result highlights the strong sensitivity of the cloud microphysics parameterization to q_{c0} and q_{i0}. As explained in detail in Part I (refer to section 2d), we had to reduce q_{c0} and q_{i0} below the values recommended by Rutledge and Hobbs (1983, 1984) and Lin et al. (1983) because of our current lack of a fractional cloudiness parameterization. The condensed water mixing ratios represent means over the whole box rather than local values over the cloudy portion of the box. Because these averages may be much smaller than the corresponding local values, we were forced to decrease q_{c0} and q_{i0} to enhance the conversion of cloud water to rain and cloud ice to snow.

The effect of increasing q_{c0} and q_{i0} on cloudiness is shown in Fig. 18. Because cloud water and supercooled cloud water form at lower altitudes than cloud ice, we expect that an increase in CW will have the largest effect on low- and middle-level cloudiness, whereas an increase in CI will mostly affect high-level clouds. Increasing q_{i0} has, by far, the largest impact on C, indicating that increasing q_{i0} leads to the formation of long-lived thin clouds (mostly high-level clouds) that would not have as long lifetimes at lower autoconversion thresholds. In contrast, increasing q_{c0} has little impact on C, indicating that the increase in CW mostly occurs over grid points that were already overcast. On a global average, the increase in q_{c0} from 0.25 to 0.7 g kg^{-1} and q_{i0} from 0.01 to 0.03 g kg^{-1} yields a 0.9% and 7.6% increase in C, respectively. In QCW0, middle-level clouds increase by 1.2% in the Tropics and the middle latitudes in the winter hemisphere, whereas high-level clouds increase by 7.6% at all latitudes in QCI0. In QCI0, low- and middle-level clouds actually decrease in the Southern Hemisphere.

The impacts of increasing CW and CI on the cloud optical depth τ and the effective cloud fraction C_{ef} are best seen in Fig. 19. Latitude–height cross sections of the zonally averaged differences in τ between QCW0 and ELQJAN and between QCI0 and ELQJAN show that the increase in CW yields a significant increase in τ for middle- and low-level clouds between 40°N and 40°S. In contrast, QCI0 gives an increase in τ for high-level clouds, which is much less than the change in τ that occurs between QCW0 and ELQJAN.

The reverse is observed for C_{ef}: It varies little between QCW0 and ELQJAN, whereas it increases significantly for extratropical high-level clouds between QCI0 and ELQJAN. This difference between QCW0 and QCI0 results because the increase in the globally averaged cloud water path is about three times larger than the increase in the globally averaged cloud ice path, and the effective radius for cloud water is three times smaller than that for cloud ice. When combined, these two differences lead to a much greater enhancement of τ for water and mixed-phase clouds than for ice clouds. A large increase in the cloud optical depth between QCW0 and ELQJAN will not modify the effective cloud cover, since thick low- and middle-level clouds are already radiatively black in ELQJAN. This does not hold for the small increase in the cloud optical depth between QCI0 and ELQJAN, which in turn leads to a significant increase in C_{ef}.

Figure 20 shows the zonally averaged distributions of LWCRF and SWCRF simulated by ELQJAN, QCW0, and QCI0. There is little variation in the zonal distribution of LWCRF between QCW0 and ELQJAN, whereas QCI0 leads to an increase in LWCRF in excess of 10 W m^{-2} at all latitudes. This result is in accordance with the respective changes in C_{ef} between QCW0 and ELQJAN and between QCI0 and ELQJAN. The increased infrared emissivity of tropical and extratropical high-level clouds between QCI0 and ELQJAN produces an enhanced greenhouse warming below cloud base in QCI0, hence increasing the LWCRF. Both QCW0 and QCI0 yield increases in SWCRF on the order of 20 W m^{-2} along the equator. QCI0 also yields a 20 W m^{-2} increase in SWCRF over the Southern Ocean. In both experiments, the increase in SWCRF results because of the increased τ of middle- and high-level clouds, as shown in Fig. 18. Despite the fact that

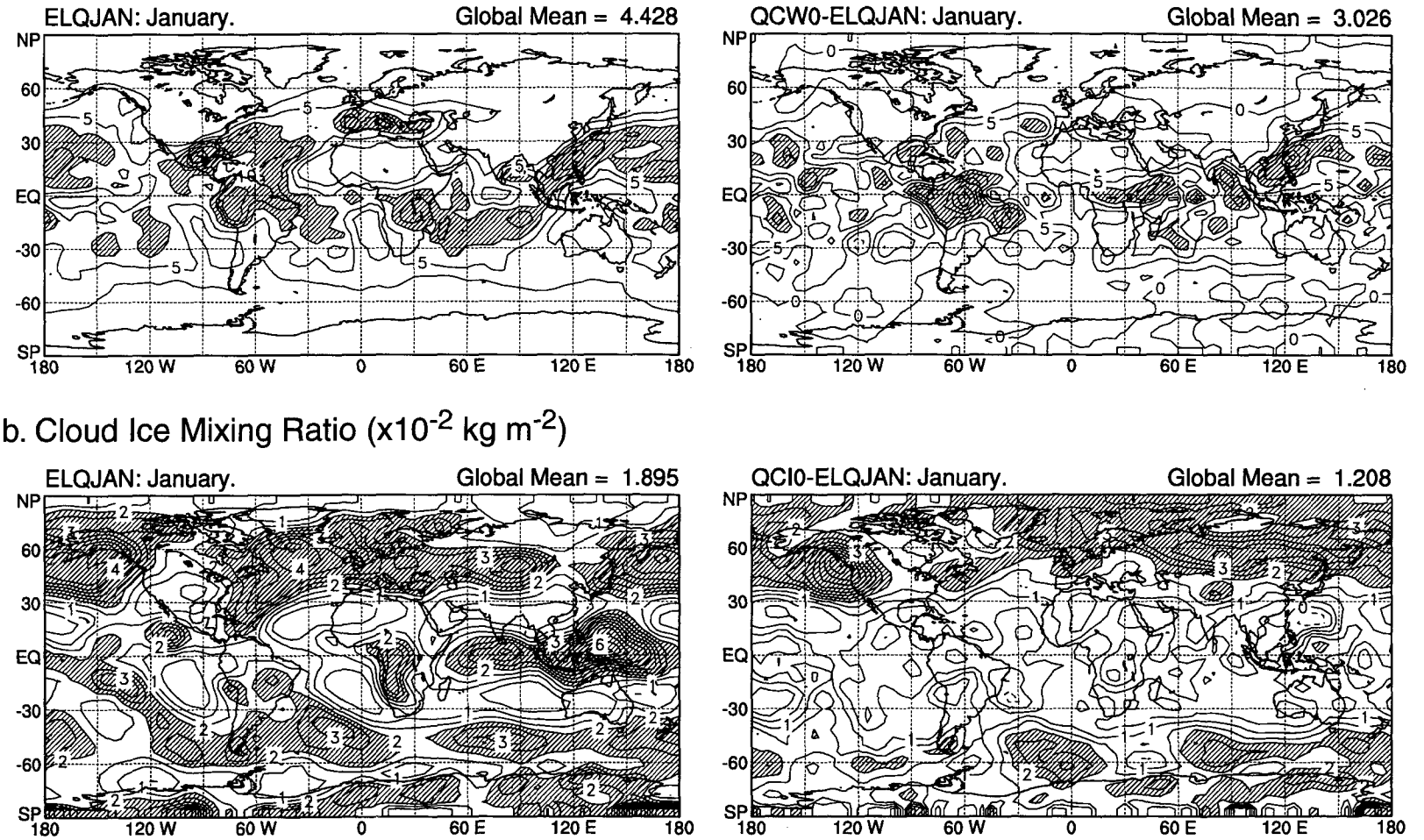

FIG. 17. Global maps of (a) the vertically integrated cloud water path simulated by ELQJAN and its difference between QCW0 and ELQJAN and (b) the vertically integrated cloud ice path simulated by ELQJAN and its difference between QCI0 and ELQJAN. Units are 10^{-2} kg m^{-2}. In (a) contour intervals are every 2.5×10^{-2} kg m^{-2}. Heavy shading corresponds to values greater than 7.5×10^{-2} kg m^{-2}. In (b) contour intervals are every 0.5×10^{-2} kg m^{-2}. Heavy shading corresponds to values greater than 2×10^{-2} kg m^{-2}.

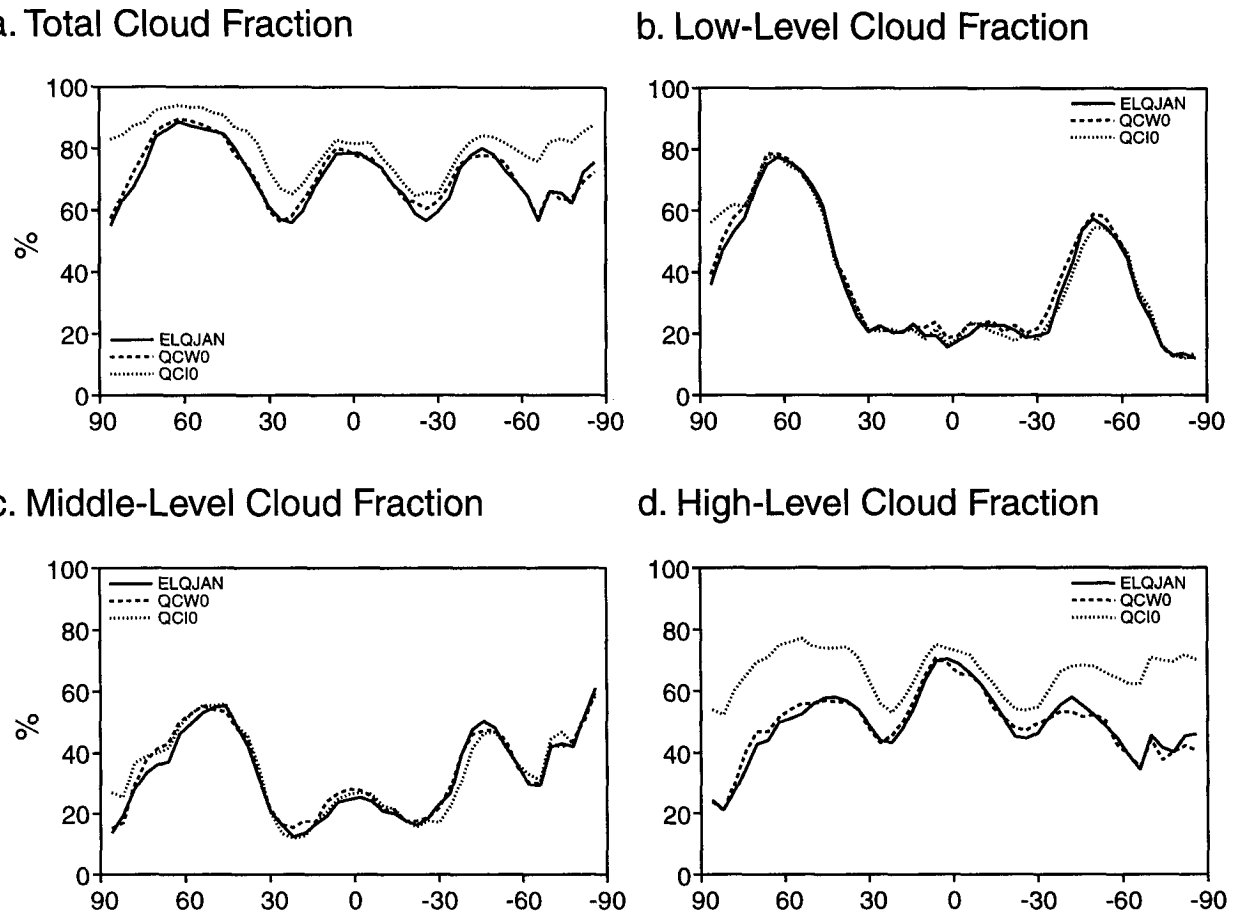

FIG. 18. Zonally averaged distributions of (a) the total cloud fraction, (b) low-level cloud fraction, (c) mid-level cloud fraction, and (d) high-level cloud fraction simulated by ELQJAN (solid line), QCW0 (dashed line), and QCI0 (dotted line). Units are percent.

the τ of tropical low- and middle-level clouds increases much more between QCW0 and ELQJAN than the τ of high-level clouds does between QCI0 and ELQJAN, the SWCRF simulated by QCW0 is not as large along the equator as that simulated by QCI0. The reason is that, in QCW0, the SWCRF of middle-level clouds is reduced by the presence of high-level clouds above.

As in the RAINOUT experiment, QCI0 shows the radiative effects of high-level clouds on the ARC and the precipitation. There is little variation in the magnitude of the precipitation between QCW0 and ELQJAN, especially in the Tropics, because the ARC remains the same in both experiments since there are no significant variations in the total cloudiness (0.9%). In QCW0, the ARC is 113.5 W m^{-2} versus 113.4 W m^{-2} in ELQJAN. In particular, we did not find any significant variations in the amount of high-level clouds (-0.2%) to which the ARC is most sensitive. The globally averaged precipitation rate simulated in QCW0 is 3.71 mm day^{-1} versus 3.68 mm day^{-1} in ELQJAN.

This is not the case in QCI0, for which the globally averaged precipitation rate decreases to 3.40 mm day^{-1} in response to a decrease in the ARC of 9.0 W m^{-2} as shown in Fig. 21. The decrease in precipitation occurs in the Tropics and the middle latitudes of the summer hemisphere. This interaction between high-level clouds, the ARC, and cumulus precipitation has been discussed by Fowler and Randall (1994) on the basis of the results of an extreme scenario in which q_{i0} was set to 0.1 g kg^{-1}, as recommended by Lin et al. (1983). In the study of Fowler and Randall (1994), they found that cumulus precipitation almost completely stopped due to an optically thick ice cloud shield, which reduced the ARC and radiatively warmed the upper troposphere.

8. Snow effects

The experiments BERG40 and NOBERG demonstrate the importance of supercooled cloud water for the partitioning between cloud water and cloud ice and

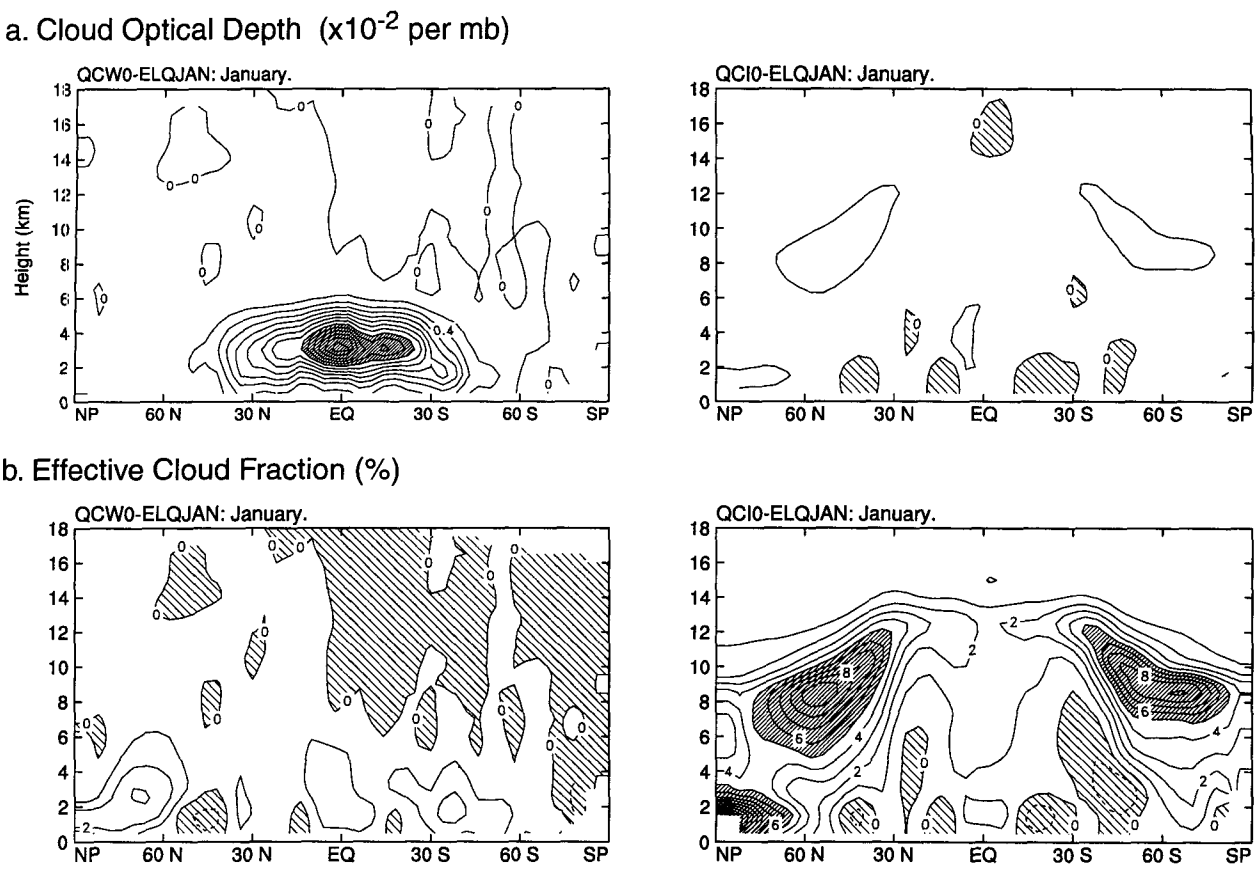

FIG. 19. Latitude–height cross sections of the zonally averaged differences in (a) the cloud optical depth and (b) the effective cloud fraction between QCW0 and ELQJAN (left panels) and between QCI0 and ELQJAN (right panels). In (a) contour intervals are every 0.2×10^{-2} per mb. Light shading corresponds to values less than 0, and heavy shading corresponds to values greater than 1.6×10^{-2} per mb. In (b) contour intervals are every 1%. Light shading corresponds to values less than 0, and heavy shading corresponds to values greater than 5%.

the top-of-the-atmosphere cloud radiative forcing. An important microphysical process linked to the formation of supercooled cloud water is its removal by falling snow in the temperature window, $-20°C \leq T < 0°C$. In the experiment PSACW, the collection of supercooled cloud water by snow is turned off. As discussed in Part II, we decided to take into account the optical properties of snow because, in the model results, RI is the most abundant water species after water vapor. In the experiment NORAD, we neglected the longwave and shortwave radiative effects of snow.

Figure 22 shows the latitude–height cross sections of the zonally averaged differences in CW and RI between PSACW and ELQJAN. Supercooled cloud water increases over the major source areas of cloud water, that is, in the Tropics at about 8 km, in the middle latitude storm tracks of the Northern Hemisphere, and over the Southern Ocean; RI also increases along the equator and in the winter hemisphere. In the experiment PSACW, autoconversion is the only microphysical process that creates snow at the expense of supercooled cloud water, and the rate of change of cloud water to snow due to autoconversion is greater than that due to collection. The increase in CW between PSACW and ELQJAN is substantial. On a global average, CW increases from 0.044 kg m^{-2} in ELQJAN to 0.097 kg m^{-2}, which stresses the importance of supercooled cloud water formation and its parameterized interactions with the other water species.

Latitude–height cross sections of the zonally averaged differences in τ and C_{ef} between PSACW and ELQJAN and between NORAD and ELQJAN are plotted in Fig. 23. In PSACW, the increased supercooled cloud water naturally leads to an increase in τ and C_{ef}, whereas NORAD mostly yields a decrease in both quantities except at low altitudes along the equator. As may be seen in Fig. 24, the impact of neglecting collection of supercooled cloud water by snow on the radiative forcing of clouds is quite striking, especially at short wavelengths. Over the Southern Ocean, the difference in SWCRF between PSACW and ELQJAN reaches 60 W m^{-2}. On a global average, OLR decreases by 4.9 W m^{-2}, whereas α increases by 4.5% in PSACW. To neglect the radiative effect of snow has

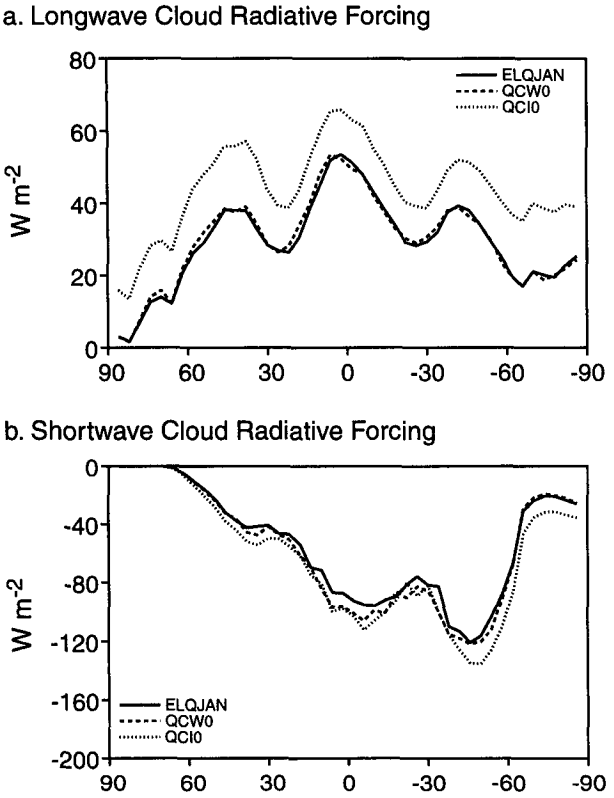

FIG. 20. Zonally averaged distributions of the top-of-the-atmosphere longwave and shortwave cloud radiative forcings simulated by ELQJAN (solid line), QCW0 (dashed line), and QCI0 (dotted line). Units are W m^{-2}.

much less impact on the simulated radiation budget quantities. The globally averaged OLR increases by 2.3 W m^{-2}, whereas α decreases by 0.95% in NORAD.

9. Summary and conclusions

We have investigated the sensitivity of the January climate simulated by the CSU GCM to some aspects of the cloud microphysics parameterization described in Parts I and II. In particular, we investigated the coupling between convection and stratiform cloudiness through the cumulus detrainment of cloud water and cloud ice, the temperature range over which mixed-phase clouds are predicted to form, and the thresholds for autoconversion of cloud water to rain and cloud ice to snow. All of the sensitivity experiments described above led to differences in the distributions of the cloud water, cloud ice, rain, and snow, which in turn modified cloudiness and its optical properties. The longwave and shortwave cloud radiative forcings changed accordingly. The sensitivity of the simulated climate to a change in the cloud microphysics parameterization emphasizes the importance of validating the distributions of cloud water, cloud ice, rain, and snow against global and regional observations. This point was discussed at great length in Parts I and II. In doing so, strengths and weaknesses of the cloud microphysics parameterization can be further identified, and one can then decide if a more detailed representation of some microphysics processes, such as the inclusion of a prognostic equation of the number concentration, is actually needed in the CSU GCM.

The three most interesting sensitivity experiments dealt with the impact of supercooled cloud droplets and the thresholds for autoconversion of cloud water to rain and cloud ice to snow

In our parameterization, the partitioning between supercooled cloud droplets and ice crystals is parameterized in a highly simplified manner as a function of the temperature. Once supercooled cloud water is formed, its only interaction with the other water species is with snow through autoconversion and collection. Supercooled cloud water indirectly interacts with cloud ice when the temperature changes. It can also become cloud water if the temperature rises above the melting level. Using this simplistic representation of the Bergeron–Findeisen mechanism, we find that changing the partitioning between supercooled cloud water and cloud ice has a significant impact upon the longwave and shortwave radiative forcings of clouds due to the difference in the cloud optical properties between mixed-phase and ice clouds. Also, the collection of supercooled cloud water by snow is a very efficient sink of cloud water that, in turn, affects the cloud radiative forcing. More research is needed to improve our understanding of the role of mixed-phase clouds in the general circulation, and more detailed microphysical processes should be added to allow more realistic interactions among supercooled cloud water, cloud ice, and snow.

An additional significant result described here was the decrease in precipitation in response to variations of the ARC. An interesting aspect of the different sensitivity experiments, considered collectively, is the relationship between the variations in the high-level

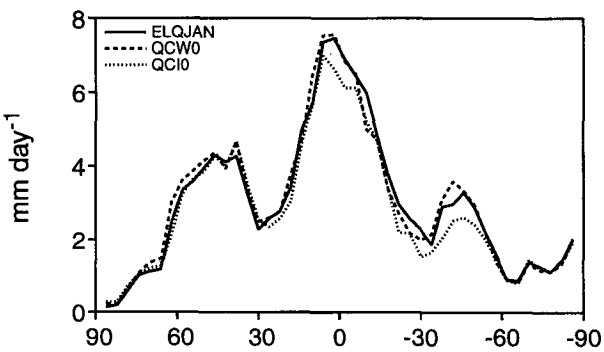

FIG. 21. Zonally averaged distribution of the precipitation simulated by ELQJAN (solid line), QCW0 (dashed line), and QCI0 (dotted line). Units are millimeters per day.

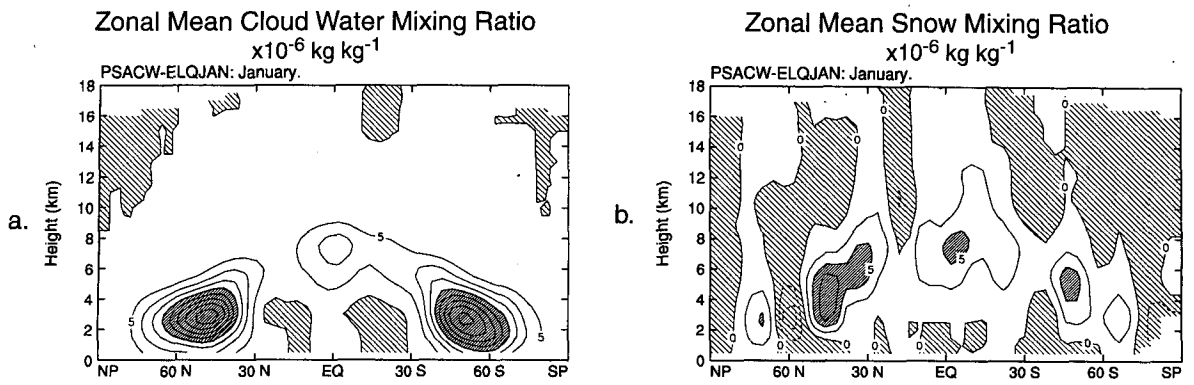

FIG. 22. Latitude–height cross sections of the zonally averaged differences in (a) the cloud water mixing ratio and (b) snow mixing ratio between PSACW and ELQJAN. In (a) contour intervals are every 5×10^{-6} kg kg^{-1}. Light shading corresponds to values less than 0, and heavy shading corresponds to values greater than 20×10^{-6} kg kg^{-1}. In (b) contour intervals are every 2.5×10^{-6} kg kg^{-1}. Light shading corresponds to values less than 0, and heavy shading corresponds to values greater than 5×10^{-6} kg kg^{-1}.

cloud amount, the ARC, and the total precipitation rate in response to changes in the cloud microphysics parameterization. Figure 25 shows a scatter diagram of the globally averaged ARC versus the globally averaged precipitation rate, which we have expressed here as a latent heat flux. Because, in the global means, the

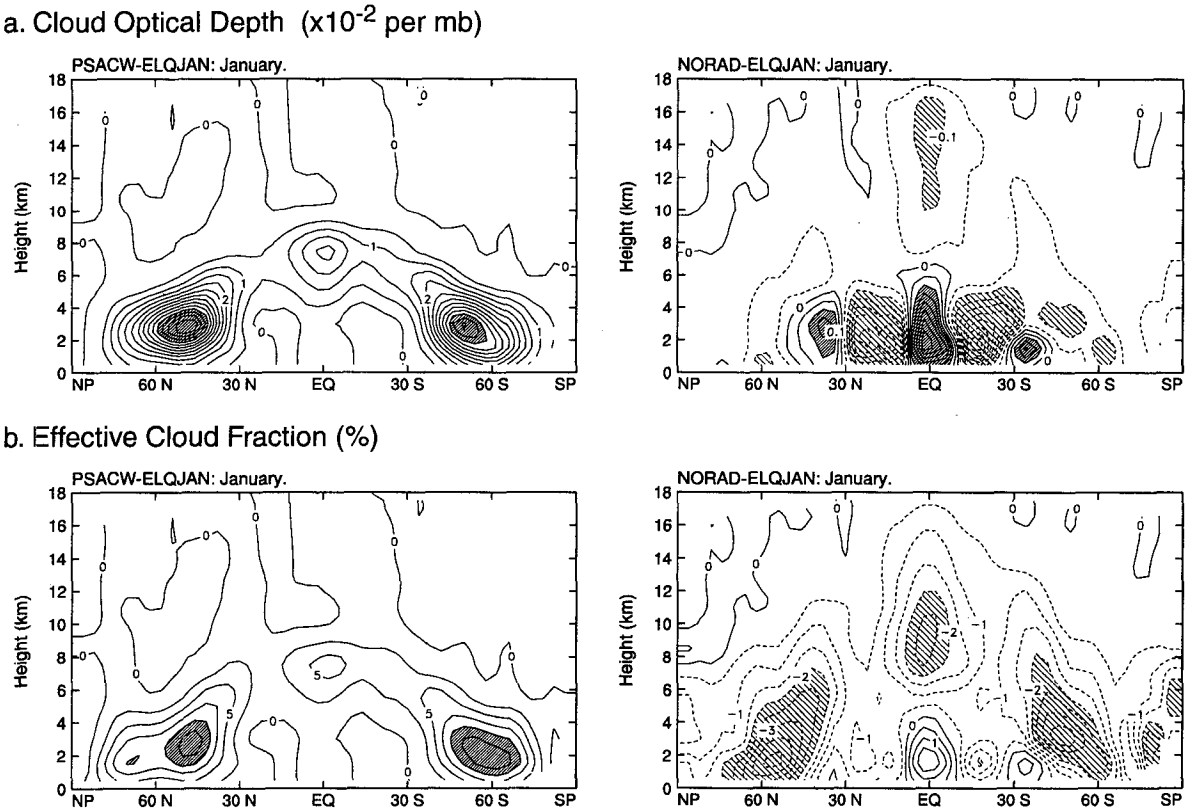

FIG. 23. Latitude–height cross sections of the zonally averaged differences in (a) the cloud optical depth and (b) effective cloud fraction between PSACW and ELQJAN (left panels) and between NORAD and ELQJAN (right panels). In (a) contour intervals are every 0.5×10^{-2} per mb (left panel) and every 0.05×10^{-2} per mb (right panel). In the left panel, heavy shading corresponds to values greater than 5×10^{-2} per mb. In the right panel, light shading corresponds to values less than -0.1×10^{-2} per mb, and heavy shading corresponds to values greater than 0.1×10^{-2} per mb. In (b) contour intervals are every 2.5% in the left panel and every 0.5% (right panel). In the left panel, heavy shading corresponds to values greater than 10×10^{-2} per mb. In the right panel, light shading corresponds to values less than -2×10^{-2} per mb.

sensible heat flux is much smaller than the latent heat flux, its contribution is minor. Each number represents one of the experiments listed in Table 1. As shown in Fig. 25, we find a linear relationship between the ARC and the precipitation rate in response to variations in cloudiness, especially high-level clouds. We also find a near balance between the ARC and the latent heating. In a sense, this is a trivial result; it just shows that the model conserves energy. Nevertheless, it illustrates the important fact that changes in cloud radiation properties can alter the global hydrologic cycle. [See Fowler and Randall (1994) for further discussion.]

The combination of the low spatial resolution of the CSU GCM and its lack of a fractional cloudiness parameterization forced us to tune the thresholds of autoconversion of cloud water to rain and cloud ice to snow to hinder the formation of optically thick cloud shields, which would lead to unrealistically low outgoing infrared radiation and unrealistically high planetary albedo. This weakness of our model was discussed at length in Parts I and II.

The differences between the sensitivity experiments and the control run in terms of the partitioning between the water species, cloudiness, and the cloud radiative forcing are certainly influenced by our current lack of a parameterization of the subgrid fractional cloudiness. The thresholds for autoconversion of cloud water to rain and cloud ice to snow are important examples of parameters that fractional cloudiness may strongly affect. We plan to reinvestigate the sensitivity of our results to the formulation of our cloud microphysics parameterizations, once fractional cloudiness has been implemented in the CSU GCM.

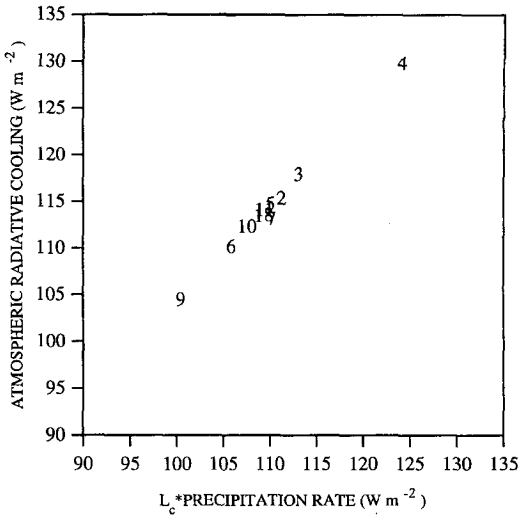

FIG. 25. Scatter diagram between the precipitation rate times the latent heat of condensation and the atmospheric radiative cooling simulated by the different experiments listed in Table 1. Numbers refer to the sensitivity experiment listed in Table 1. The slope and ordinate of the inferred regression line are 1.065 W m^{-2} and −2.824 W m^{-2}, respectively.

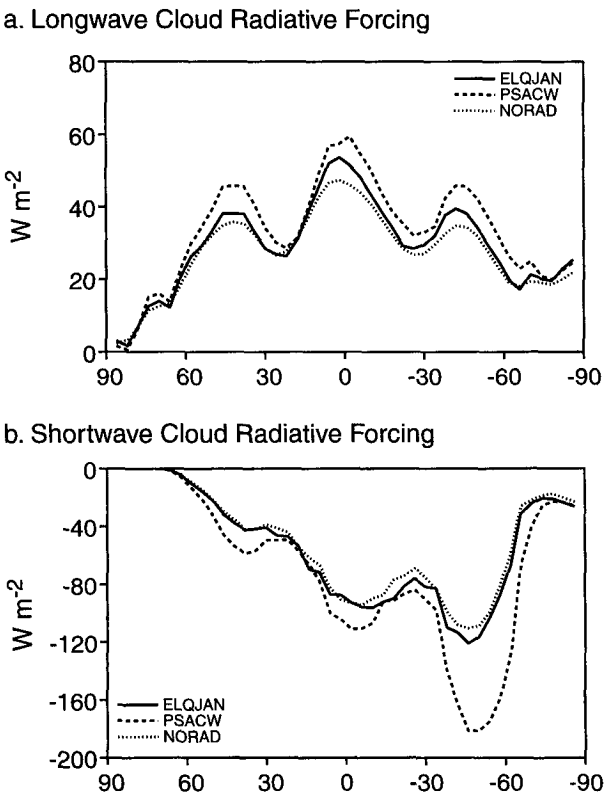

FIG. 24. Zonally averaged distributions of the top-of-the-atmosphere (a) longwave cloud radiative forcing, and (b) shortwave cloud radiative forcing simulated by ELQJAN (solid line), PSACW (dashed line), and NORAD (dotted line). Units are W m^{-2}.

Acknowledgments. This research was sponsored by the National Science Foundation under Grant ATM-8907414, by NASA under Grant NAG-1-1266, and by the ARM program of the U.S. Department of Energy under Grant DE-FG02-92ER61363, which were all to Colorado State University. Research was also sponsored by Subcontract 0965G4A007 from the University of California Los Angeles, under NASA Grant NAG 5-2224. Computing resources were provided by the Scientific Computing Division at the National Center for Atmospheric Research, by the National Center for Computational Sciences at NASA/Goddard, and by the National Energy Research Supercomputer Center at Lawrence Livermore National Laboratory.

REFERENCES

Arakawa, A., and W. H. Schubert, 1974: The interactions of a cumulus cloud ensemble with the large-scale environment, Part I. *J. Atmos. Sci.*, **31**, 674–701.

Barkstrom, B. R., and G. L. Smith, 1986: The Earth Radiation Budget Experiment: Science and implementation. *J. Geophys. Res.*, **24**, 379–390.

Del Genio, A. D., and M.-S. Yao, 1989: Prediction of cloud water variations in the GISS GCM. Preprints, *Conf. on Cloud Physics,* San Francisco, CA, Amer. Meteor. Soc., 497–504.

Fowler, L. D., and D. A. Randall, 1994: A global-radiative-convective feedback. *Geophys. Res. Lett.,* **21,** 2035–2038.

——, and ——, 1996: Liquid and ice cloud microphysics in the CSU general circulation model. Part II: Impact on cloudiness, the earth's radiation budget, and the general circulation of the atmosphere. *J. Climate,* **9,** 530–560.

——, and ——, and S. A. Rutledge, 1996: Liquid and ice cloud microphysics in the CSU general circulation model. Part I: Model description and simulated cloud microphysical processes. *J. Climate,* **9,** 489–529.

Greenwald, T. J., G. L. Stephens, T. H. Vonder Haar, and D. L. Jackson, 1993: A physical retrieval of cloud liquid water over the global oceans using Special Sensor Microwave/Imager (SSM/I) observations. *J. Geophys. Res.,* **98,** 18 471–18 448.

Gunn, K. L. S., and G. D. Kinzer, 1949: The terminal velocity of fall for water droplets in stagnant air. *J. Meteor.,* **6,** 243–251.

——, and J. S. Marshall, 1958: The distribution with size of aggregate snow flakes. *J. Meteor.,* **15,** 452–461.

Harshvardhan, R. Davies, D. A. Randall, and T. G. Corsetti, 1987: A fast radiation parameterization for atmospheric general circulation models. *J. Geophys. Res.,* **92,** 1009–1016.

——, D. A. Randall, T. G. Corsetti, and D. A. Dazlich, 1989: Earth radiation budget and cloudiness simulations with a general circulation model. *J. Atmos. Sci.,* **46,** 1922–1942.

Kessler, E., III, 1969: *On the Distribution and Continuity of Water Substance in Atmospheric Circulations. Meteor. Monogr.,* No. 32, Amer. Meteor. Soc., 84 pp.

Lin, Y.-L., R. D. Farley, and H. D. Orville, 1983: Bulk parameterization of the snow field in a cloud model. *J. Climate Appl. Meteor.,* **22,** 1065–1092.

Locatelli, J. D., and P. V. Hobbs, 1974: Fallspeeds and masses of solid precipitation particles. *J. Geophys. Res.,* **79,** 2185–2197.

Ose, T., 1993: An examination of the effects of explicit cloud water in the UCLA GCM. *J. Meteor. Soc. Japan,* **71,** 93–109.

Randall, D. A., 1989: Cloud parameterization for climate modeling: Status and prospects. *Atmos. Res.,* **23,** 341–361.

——, and D.-M. Pan, 1993: Implementation of the Arakawa–Schubert cumulus parameterization with a prognostic closure. *The Representation of Cumulus Convection in Numerical Models, Meteor. Monogr.* No. 46 Amer. Meteor. Soc., 137–144.

Rood, R. B., 1987: Numerical advection algorithms and their role in atmospheric transport and chemistry models. *Rev. Geophys.,* **25,** 71–100.

Rutledge, S. A., and P. V. Hobbs, 1983: The mesoscale and microscale structure and organization of clouds and precipitation in midlatitude cyclones. VIII: A model for the "Seeder-Feeder" process in warm-frontal rainbands. *J. Atmos. Sci.,* **40,** 1185–1206.

——, and ——, 1984: The mesoscale and microscale structure and organization of clouds and precipitation in midlatitude cyclones. XII: A diagnostic modeling study of precipitation development in narrow cold-frontal rainbands. *J. Atmos. Sci.,* **41,** 2949–2972.

Senior, C. A., and J. F. B. Mitchell, 1993: Carbon dioxide and climate: The impact of cloud parameterization. *J. Climate,* **6,** 393–417.

Suarez, M. J., A. Arakawa, and D. A. Randall, 1983: Parameterization of the planetary boundary layer in the UCLA general circulation model: Formulation and results. *Mon. Wea. Rev.,* **111,** 2224–2243.